FINAL REPORT

Improving Magnetic Flux Leakage In-Line Inspection Corrosion Sizing using Focused Guided Ultrasonic Waves

By
J. Bruce Nestleroth
Energy Systems & Carbon Management
Battelle Memorial Institute
505 King Avenue
Columbus, OH 43201
nestlero@battelle.org

Jason K. Van Velsor
FBS, Inc.
3340 West College Ave.
State College, PA 16801
jvanvelsor@fbsworldwide.com

Prepared for
U.S. Department of Transportation
Pipeline and Hazardous Materials
Safety Administration
1200 New Jersey Ave., SE
Washington DC 20590
Contract No. DTPH56-08-T-000004, Project 232
Battelle Project No. G006084

Conoco Inc.
600 N. Dairy Ashford
Houston TX 77079-1175
Contract: ID# SALAMMM
Battelle Project No. N105348

September 30, 2010

This report is a work prepared for the United States Government by Battelle. In no event shall either the United States Government or Battelle have any responsibility or liability for any consequences of any use, misuse, inability to use, or reliance upon the information contained herein, nor does either warrant or otherwise represent in any way the accuracy, adequacy, efficacy, or applicability of the contents hereof.

Battelle does not engage in research for advertising, sales promotion, or endorsement of our clients' interests including raising investment capital or recommending investment decisions, or other publicity purposes, or for any use in litigation. Battelle endeavors at all times to produce work of the highest quality, consistent with our contract commitments. However, because of the research or experimental nature of this work, the client undertakes the sole responsibility for the consequences of any use or misuse of, or inability to use, any information, apparatus, process, or result obtained from Battelle, and Battelle, its employees, officers, or Directors have no legal liability for the accuracy, adequacy, or efficacy thereof.

Approved:

Glenda Holderbaum, Manager
Energy Systems & Carbon Management

Public Abstract

In-line inspection is an integral part of many pipeline company integrity management plans. The most common inspection technology for both natural gas and liquid pipelines is magnetic flux leakage (MFL). MFL was first used in the 1960's and was significantly improved in the 1980's and 1990's. While improvements are still being implemented, the performance capability of MFL tools has remained relatively unchanged for a decade. The major attribute of MFL is the ruggedness of the implementations that enable this technology to perform under the rigors presented by the pipeline environment. The most commonly reported deficiency of this technology is the lack of precision in reported sizes of the anomalies detected. The nominal depth sizing specification of most MFL in-line tools is a tolerance of +/-10% of wall thickness with a certainty of 80% (4 of 5 depth readings are within the tolerance). The depth of long narrow axially aligned anomalies are particularly problematic.

The goal of this development is to improve corrosion anomaly depth sizing of MFL tools by adding a second complimentary technology, focused guided-wave ultrasonic inspection technology. An electromagnetic acoustic transducer (EMAT) sensor was developed to generate and receive the focused ultrasonic energy at the anomaly. The design has been tested in the laboratory and on pipe pulled from service at the Pipeline Simulation Facility. This EMAT sensor uses focusing to provide better resolution of the ultrasonic waves over commercially available implementations of EMATS used for pipeline inspection. Since anomalies are typically smaller than the lateral resolution of common sensors, detection can be good but sizing will be a challenge. Focusing of the guided waves generated by the EMATS can provide tight beam for interrogating pipeline anomalies.

This project resulted in new technology to augment MFL tools for improved corrosion sizing. MFL tools would still be used to detect corrosion and provide typical sizing information. The guided wave technology will provide additional information for the better characterization of depth. The configuration developed on this program primarily addressed long narrow axially aligned anomalies. The improved accuracy provided by this in-line inspection technology will help pipeline owners better assess corrosion anomalies and more accurately determine corrosion growth rates to enhance their integrity management programs.

Table of Contents

Page

1. Introduction 1
   1.1. Motivation 1
   1.2. Literature Review 2
2. Analytical Modeling of Circumferential Guided Waves 4
3. Guided Wave Focusing Implementation 7
4. Numerical Modeling of Circumferential Guided Waves 17
5. Experimental Proof of Concept 25
6. Conclusion and Future Direction 53
7. References 55

List of Tables

Table 1.1. Pros and Cons of the MFL and GWUT Technologies 2

Table 3.1. Breakdown of saved waveform file sizes with different parameters. All data in files have a precision of 3. 13

Table 3.2. Transmitting and receiving setup for synthetic focusing. 14

Table 3.3. Data acquisition times for various phased-array systems. 15

Table 5.1. Summary of results from geometrical focusing experiments 26

Table 5.2. Arbitrary Waveform Generator 32

Table 5.3. Analog-to-Digital Converter 32

Table 5.4. Toneburst Amplifier 33

Table 5.5. Defect details in the 12 *in* schedule 40 X52 verification specimen. 35

List of Figures

Figure 2.1. Phase velocity (top) and group velocity (bottom) dispersion curves for a 12 *in* diameter schedule 40 X52 steel pipe. Mode/frequency combinations of interest are circled in blue. 5

Figure 2.2. Wave structures of the two mode/frequency combinations of interests, as circled in blue in Figure 2.1. Both wave structures show sufficient energy at the inner and outer surfaces of the pipe to be used for corrosion detection and sizing. 6

Figure 3.1. Guided wave phased array concept for ILI using EMATs. 7

Figure 3.2. Lorentz EMAT transducer principle. 8

Figure 3.3. Lamb wave EMAT transducer. 8

Figure 3.4. EMAT coil configurations fabricated for laboratory testing, including (a) directionally focused coils and omni-directional (b) spiral coils and (c) labyrinth coils..... 9

Figure 3.5. Photographs showing experimental setup for omni-directional coil directionality tests. The transmitting coil was rotated 360° while the receiver remained fixed in place..... 10

Figure 3.6. Polar plots showing directionality properties of the omni-directional (a) spiral coils and (b) labyrinth coils. It is seen that both coils favor excitation in particular directions..... 11

Figure 3.7. Photograph showing the focused coil EMAT. 11

Figure 3.8. RF waveforms obtained using the different types of coils. It is seen that the (c) focused coils produced the best signal-to-noise ratio. The much weaker signals obtained from the (a) spiral and (b) labyrinth coils is expected as the energy is being transmitted in many directions as opposed to along a single line..... 12

Figure 3.9. Geometrically focused array concept showing how mechanical phasing of the individual array sensors can be used to form a focal point at a specific location..... 15

Figure 4.1. RF-waveform envelopes showing the decrease in signal amplitude as EMAT sensors are removed from the focused array. 18

Figure 4.2. Summary of results from modeling comparison of the straight, curved, and curved array sensor configurations. 19

Figure 4.3. Image showing model configuration (top) for studying the width of the focused beam profile at the focal point. The result shown on the bottom shows a highly concentrated beam at the focal point. 20

Figure 4.4. Plot of wave amplitude across the width of the plate model shown in Figure 4.3. It is seen that the 6 dB beam width is approximately 1 *in*. 21

Figure 4.5. A 456kHz S1 guided wave is generated in the circumferential direction in a 12 *in* schedule 40 X52 steel pipe by an EMAT. 0%~100% through-wall spherical defects are cut on the inner surface of the pipe as shown on the left. 22

Figure 4.6. Still frame from animations showing 456 *kHz* S1 mode being transmitted and reflected by a 60% through-wall pit-like defect. 22

Figure 4.7. Analytic wave envelopes of the reflected (left) and transmitted (right) 456 *kHz* S1 wave mode for pipe with no defects (top), with a 40% through-wall pit (middle), and with an 80% through-wall pit (bottom). 23

Figure 4.8. Plots comparing reflected (left) and transmitted (right) signal amplitude for a 456 *kHz* S1 wave impinging upon a pit-like defect with 0% to 100% through-wall depth..... 24

Figure 5.1. Photographs of experimental setup and corresponding acquired waveforms used for analysis. (a) Signal received from direct transmission of one transmitter. This signal was used

as the reference to compare the focusing results. (b) Waveform acquired when two transmitters were used to generate a focal zone. (c) Signal received from three-transmitter configuration. .. 26

Figure 5.2. RF waveform acquired after moving the receiving EMAT 3 in. past the focal point of the 3-EMAT focused array. Signal amplitude decreased by 10.14 dB confirming that the array has a focal point at the designed distance of 19 *in*. 27

Figure 5.3. Primary sensor configurations used for data acquisition using the prototype ILI tool. 27

Figure 5.4. Details of the sensor configuration and design for pulse-echo measurements using the geometrically focused array. 28

Figure 5.5. Details of sensor configuration and design used for through-transmission data acquisition. 29

Figure 5.6. Three different EMAT coil designs employed in the two ILI tool configurations. .. 30

Figure 5.7. Photographs showing the completed prototype ILI tool for data acquisition. 30

Figure 5.8. System flow chart showing key components. 31

Figure 5.9. Screenshots of waveform display software developed for processing and viewing ILI data. Top screen contains filtering settings and bottom screen shows spatial averaging options. 34

Figure 5.10. Schematic showing defect location and detail in the 12 *in* 0.375 *in* wall thickness X52 verification specimen. 35

Figure 5.11. Unfiltered and unaveraged defect amplitude data for 12-*in* verification pipe. Note that all defects are identified without the use of any signal processing. 36

Figure 5.12. Filtered and normalized amplitude data for 12-*in* verification pipe. Note that normalized amplitude information accurately ranks each defect according to depth for each defect class. The different classes can be differentiated by comparing the A0 and S1 data. 36

Figure 5.13. Three different data sets obtained from the simulated pit defects showing both amplitude and time-based detection and sizing features. 38

Figure 5.14. Three different data sets obtained from the simulated pit defects showing both frequency-based detection and sizing features. 39

Figure 5.15. Through transmission data taken on 12 in schedule 40 X52 pipe. Data shows that frequency bandwidth is an excellent detection feature. Max amplitude data shown is unfiltered and unaveraged. 40

Figure 5.16. Photographs of clean (left) and pitted (right) section of the 12 *in* schedule 40 pipe sample that was removed from service. 41

Figure 5.17. Automated ultrasonic scan of the pipe sample. 42

Figure 5.18. Photograph of ID corrosion corresponding to the boxes in Figure 5.13. 43

Figure 5.19. Pulse-echo pull data obtained on r natural corrosion pipe section. Note that the tool rotated as it was pulled through the pipe and caused the focal point to rotate out of the defect region. 44

Figure 5.20. Analytic wave envelopes from several random locations within the clean section of pipe. Note that there are no reflections in the focal region that are above the noise floor. 45

Figure 5.21. Analytic wave envelopes from several random locations within the pitted section of pipe. Note that there are obvious reflections in the focal region that are well above the noise floor. 46

Figure 5.22. Photographs of the inside pipe surface at the locations corresponding to the data sets in Figure 5.20. Note that the percentages are the depth of the pits relative to the original thickness of the pipe. 47

Figure 5.23. Through transmission pull data obtained on retired pipe section at Battelle PSF facility. 48

Figure 5.24. Through transmission analytic wave envelopes from several random locations within the clean section of pipe. Note that the amplitude of the through transmission pulse is high and very comparable at the different locations. 49

Figure 5.25. Through transmission analytic wave envelopes from several random locations within the pitted section of pipe. Note that the amplitude of the through transmission pulse is low and correlates well to the depth of the pits as indicated in Figure 5.21. 50

Figure 5.26. Photographs of the inside pipe surface at the locations corresponding to the data sets in Figure 5.24. Note that the depths of these pits are indicated in Figure 5.21. 51

Figure 5.27. Side by side comparison of focused pulse-echo (left) and through transmission (right) data sets. Note excellent correlation between defect locations and relative severity. 52

1. INTRODUCTION

1.1. MOTIVATION

Magnetic flux leakage (MFL) is the oldest and most commonly used in-line inspection (ILI) method for finding metal-loss regions in oil and natural gas transmission pipelines. Although detection is generally regarded as good, MFL is often criticized as not providing sufficient accuracy in sizing these anomalies. The depth of some anomalies are undersized leading to safety concerns while other are oversized leading to unnecessary repairs. While improvements are still being implemented, the performance capability of MFL tools has remained relatively unchanged for a decade. The major attribute of MFL is the ruggedness of the implementations that enable this technology to perform under the rigors presented by the pipeline environment. The most commonly reported deficiency of this technology is the lack of precision in reported sizes of the anomalies detected. The nominal depth sizing specification of most MFL in-line tools is a tolerance of +/-10% of wall thickness with a certainty of 80% (4 of 5 depth readings are within the tolerance).

Ultrasonic guided wave technology is an emerging inspection technology that is finding application in the oil and gas industry. One of the first commercial applications has been long-range guided wave inspection of unpiggable areas such as cased crossings and compressor stations. Improvements to these systems continue to enhance performance and expand areas of use. Attempts at using guided waves for ILI began in the 1980's; however, only in the last several years have tools been offered as a commercial service. These tools typically use electromagnetic acoustic transducers (EMATs) to generate the guided waves to inspect pipeline for axially aligned cracks such as Stress Corrosion Cracking (SCC). While MFL has two implementations for pipelines, traditional axially magnetization and more recent circumferential magnetization, EMAT can be implemented in many ways leading to a wide range of tool configurations. A fundamental aspect in implementing EMAT technology on an inspection tool is selecting the proper ultrasonic mode and frequency needed for the particular implementation. Through the proper application of theoretical wave mechanics, numerical modeling, and physically-based experimentation, guided wave ultrasound (GWUT) can be optimized by selecting the modes/frequencies with the ideal dispersion characteristics and wave structures for a particular task. The improper selection of parameters has led to EMAT systems that do not perform adequately. The ability of numerical modeling has only recently become practical for the design of systems and should lead to improved EMAT implementations.

To produce the proper mode and signal strength, the physical size of the EMAT sensors needs to be on the order of 2 to 4 inches. This large size is a physical requirement that is a function of pipe parameters such as wall thickness. Since anomalies are typically smaller than the lateral resolution of the sensor, detection can be good but sizing will be a challenge. Focusing of the guided waves generated by the EMATS can provide tight beam for interrogating pipeline anomalies.

A synergistic approach would combine the advantages (see Table 1.1) of MFL with that of a GWUT phased array and, in the process, overcome many of the disadvantages of the two traditionally independent methodologies. The result would be a more decisive, robust, and information-rich inspection system for detecting and sizing corrosion that neither of the

individual technologies is capable of independently. Therefore, the motivation and primary goal of this development is to improve corrosion anomaly depth sizing of MFL tools by adding phased array GWUT inspection technology.

Table 1.1. Pros and Cons of the MFL and GWUT Technologies

	Pros	*Cons*
MFL	▪ Excellent ILI corrosion *detection* potential ▪ Well established technology that is used by pipeline industry ▪ Relatively simplistic ▪ Rugged and robust ▪ Can inspect long distances with off the shelf components	▪ Sizing corrosion anomalies has large tolerance and low certainty ▪ Unable to detect planar defects (SCC) parallel to magnetization direction ▪ Mature technology with limited room for improvement
GWUT	▪ Excellent for both defect *location* and *sizing* ▪ Capable of detecting planar defects (SCC) ▪ Variable defect sensitivity	▪ Inflated data storage requirements ▪ Many Options. Requires advanced understanding of wave mechanics for successful application ▪ Increased power consumption

1.2. LITERATURE REVIEW

When the nearest boundaries of a structure are comparable to the wavelength of a wave traveling in the structure, complex interference patterns are created. When the interference is constructive, guided waves are formed and can propagate for long distances. Several examples of the thousands of applications involving guided waves include defect detection, location, and sizing, material characterization, ice detection and removal, and quantitative measurement of structural dimensions, fluid viscosity, and flow rate.

Guided wave propagation in the axial direction of pipe has been studied thoroughly with much of the early theoretical work completed by Ghosh (1), Mirsky and Herrmann (2, 3), and Gazis (4, 5) in the early-to-mid 20th century, and the first experimental work was demonstrated by Zemanek (6) in the 1970's. More recently Li and Rose (7, 8, 9) and Sun et al. (10) have completed the theoretical development and demonstration of guided wave focusing in the axial direction of pipe. Focusing refers to the ability to create constructive interference at a specific axial and circumferential location, and it greatly enhances defect detection and sizing capabilities.

Compared to the available library regarding axial wave propagation, the material available regarding circumferential wave propagation is relatively terse. Viktorov (11) first addressed the topic of Lamb-type wave propagation in the circumferential direction of a circular annulus. He defined the concept of angular wave number, which is a unique physical phenomenon of guided waves traveling in curved space. Liu and Qu (12) and Zhao and Rose (13) were the first to

present the dispersion solutions for Rayleigh-Lamb-type and shear-horizontal waves, respectively. Chapter 12 of Rose (14) also addresses this topic. Some applications involving circumferential guided waves (CGWs) include those developed by Valle et al. (15) for crack detection and sizing, by Van Velsor et al. (16) for coating disbond detection, by Hirao and Ogi (17) for corrosion detection and sizing, and by Satyarnarayan et al. (18) for pinhole detection and sizing in pipe support regions.

Also, Liu and Qu (19) studied transient circumferential wave propagation using the Normal Mode Expansion technique. Li and Berthelot (20) used the work of Liu and Qu (19) to determine the optimal angle-of-incidence for the detection of radial cracking on the inner surface of an annulus. Valle, Niethammer (15) also studied radial crack detection and sizing using Lamb-type circumferential waves. Valle et al. (21) addressed the propagation of circumferential Lamb-type waves in a solid shaft within a single cylindrical layer, but because of the highly specialized structural geometry, boundary, and interfacial continuity conditions, the presented solution is not applicable to multilayered hollow cylinders. Towfighi et al. (22) and Jiandong et al. (23) used Fourier series and Legendre polynomials, respectively, to solve the coupled governing differential equations encountered for circumferential Lamb-type wave propagation in single-layered anisotropic media.

In addition to the cited refereed journal publications, there have been several industrial research projects that have addressed topics similar to that of the present work. Nestleroth and Alers (24) studied the topic of disbond detection using guided waves implemented with ILI tools. In their work, EMATs were employed using the magnetic field present from an MFL tool to generate guided Lamb-type waves, which propagated along the axial direction of the pipe. Signal amplitude was the single discretionary feature for coating disbond detection. Disbond detection was realized but it was determined that other detection features were needed for a more reliable inspection. Also, the technique did not work as well for thinner coatings such as Fusion Bonded Epoxies (FBEs). More recent work by Nestleroth and Van Velsor (25) have added robustness to the coating disbond detection capability by identifying additional detection features other than amplitude and demonstrated the technique for both coal-tar type coatings and FBEs.

Aaron et al. (26) studied the detection and sizing of SCC using EMATs deployed from an ILI tool. A Magnetostrictive EMAT technique was employed to generate circumferentially traveling Shear-Horizontal and Shear-Vertical guided waves. A bench scale ILI tool was constructed and used to perform sizing studies on SCC. Coating disbondment was not addressed. Al-Qahtani et al. (27) demonstrated a fully operational EMAT tool for the detection of SCC and coating disbondment detection. A SH-wave technique was employed but, as was the case in the work done by Nestleroth and Alers (24), signal amplitude was the only contrast mechanism used for coating disbondment detection.

2. ANALYTICAL MODELING OF CIRCUMFERENTIAL GUIDED WAVES

Theoretical and numerical modeling are invaluable tools as they can be used to predict the expected behavior of ultrasonic waves propagating in a bounded structure. By comparing this expected behavior with the behavior observed by experiment, it is possible to correlate certain features to structural variations such as corrosion. For this effort, the primary goal of the analytical modeling was to select potential modes and frequencies that have the best potential for implementation with a phased-array focusing approach and that can be reliably correlated, by some feature, to the geometry and depth of elongated and pit-like corrosion anomalies. The capability to model ultrasonic guided waves has only become practical in the past few years and this enabling technology is necessary for the development of robust EMAT implementations. This parallels the advancing of MFL in the 1980's and 1990's, where magnetic modeling methods became practical and high resolution MFL became the industry standard.

Toward this goal, it was determined that circumferential Lamb-Type (CLT) waves provided the most potential for providing sizing information for the following reasons:

- High sensitivity to corrosion type anomalies.
- More propagating modes mean more possible detection and characterization features. Although, this also means that extreme care needs to be taken in selecting the excitation mode and frequency.
- Ability to construct EMAT sensors that can be used for phased-array focusing. Geometric limitations of Horizontal Shear type EMATs make them less conducive to building a probe that can be used in a phased-array and focused at many different locations.
- In the frequency ranges of most interest here, the CLT wave modes have relatively lower attenuation rates than Circumferential Shear Horizontal (CSH) waves. This translates to longer propagation distances and better signal-to-noise ratios for applications involving coated pipe.

Figure 2.1 shows the phase and group velocity dispersion curves for a 12-*in* diameter Schedule 40 X52 steel pipe. The phase velocity represents the speed at which a single wave travels while the group velocity represents the speed at which a group of waves, or wave packet, travels. For sensor design, the phase velocity dispersion curves are of the most interest. Most often in experiments, the group velocity is the value being measured and therefore it is necessary to consider both sets of curves.

Of particular interest in the phase velocity dispersion curves of Figure 2.1 are mode regions with relatively low dispersion, in other words, mode regions where phase velocity does not change significantly with frequency. Selecting these modes ensures that a coherent wave packet will be maintained, as all the individual waves in the wave group will be traveling at nearly the same speed. Another consideration to be made is the type of sensor that will be used to excite the wave. For this work, EMATs will be used for the ILI application. This type of sensor has a fixed wavelength and will therefore be capable of exciting only wave mode/frequency combinations that lie along a diagonal activation line, as shown in the phase velocity dispersion curves in Figure 2.1. By adjusting the wavelength of the sensor, it can be made to excite a mode or modes that are desirable for a particular application.

The desired activation line seen in the phase velocity dispersion curves in Figure 2.1 has been selected such that the Circumferential A0 (CA0) and Circumferential S1 (CS1) modes can be excited at frequencies of 200 *kHz* and 456 *kHz*, respectively. These regions are indicated by the blue circles and represent regions with low dispersion rates. Again, by selecting this activation line it will be possible to excite both modes using the same EMAT sensor configuration.

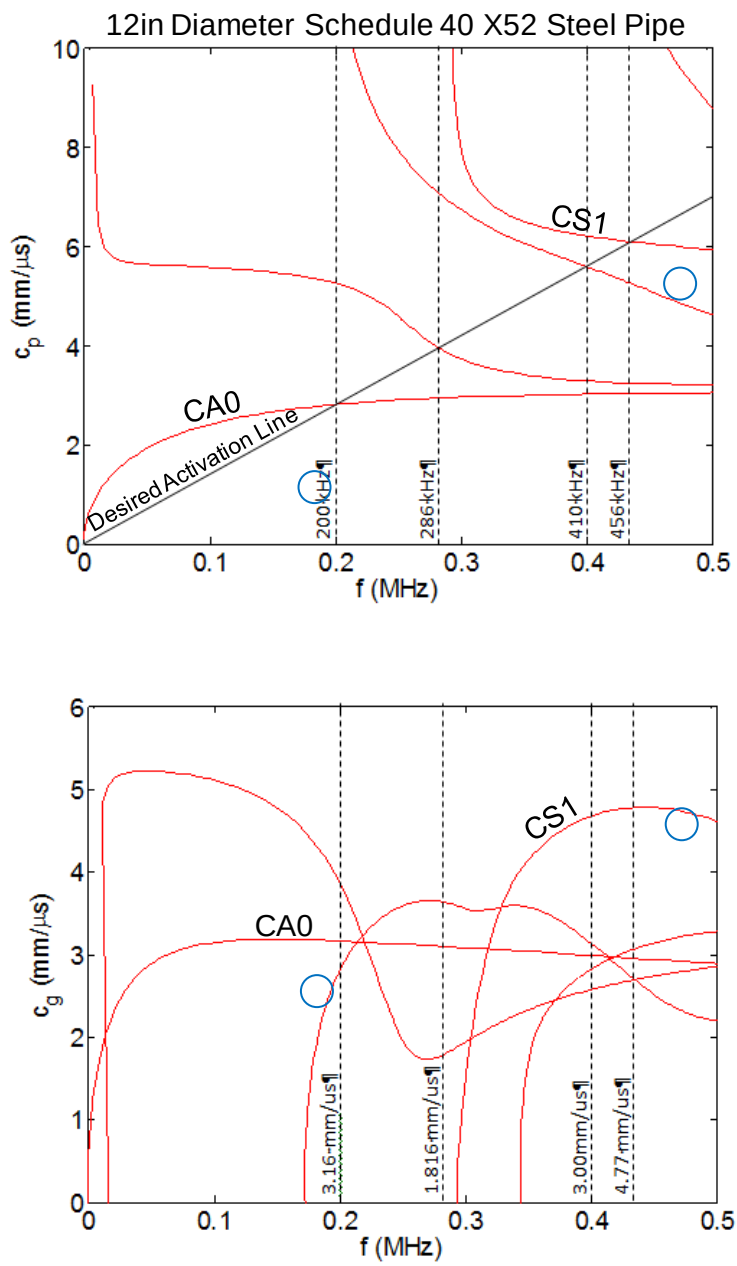

Figure 2.1. Phase velocity (top) and group velocity (bottom) dispersion curves for a 12-*in* diameter schedule 40 X52 steel pipe. Mode/frequency combinations of interest are circled in blue.

Figure 2.2 shows the wave structures corresponding to the two mode/frequency combinations highlighted in Figure 2.1. From these wave structures it is seen that both modes have sufficient energy content at the inner and outer surfaces of the pipe to be used for corrosion detection and sizing. The CA0 mode has dominant out-of-plane (u_r) displacement and the CS1 mode has dominant in-plane (u_θ) displacement. It must now be demonstrated that these modes can be employed with the focusing technique in a predictable manner to provide sizing information for corrosion defects. Due to the complex geometries of corrosion defects, this problem was investigated using numerical models rather than analytical solutions. This is the focus of Section 4. The next section, Section 3, discusses the guided wave focusing concept and implementation plan for the ILI tool.

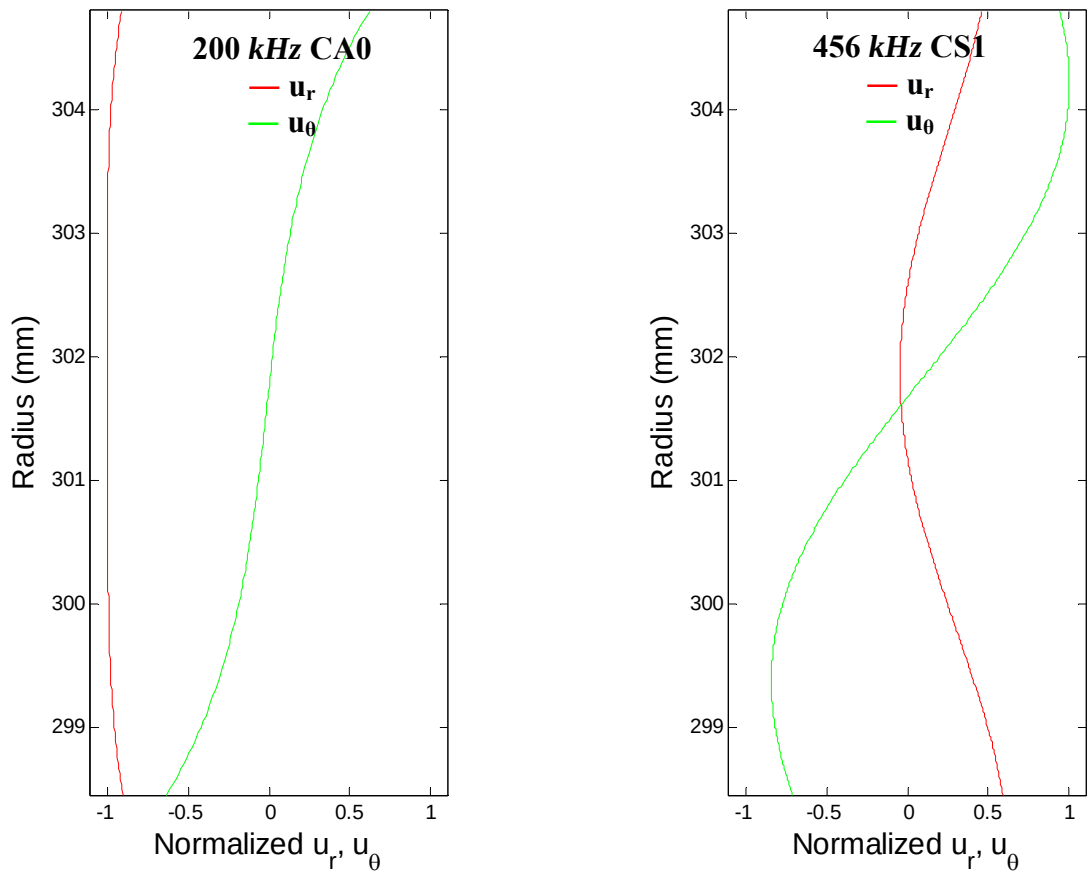

Figure 2.2. Wave structures of the two mode/frequency combinations of interests, as circled in blue in Figure 2.1. Both wave structures show sufficient energy at the inner and outer surfaces of the pipe to be used for corrosion detection and sizing.

3. GUIDED WAVE FOCUSING IMPLEMENTATION

In this section, the guided wave focused array concept and implementation plan is discussed. Figure 3.1 shows an illustration of the GWUT phased-array concept, as it would be applied on an ILI tool. In this illustration, an array of sensors is shown focusing energy at a point just in front of a defect. By adjusting the time between pulses sent by each sensor it is possible to steer the focal point to different areas in the pipe wall Rose (28). When scanning in the circumferential direction of a pipe, GWUT phased-array theory is a combination of guided-wave mechanics and phased-array radar theory. The focused beam is determined from the sum of the weighted contribution from each individual sensor. In mathematical form this is,

$$z(\mathbf{r},t) = \sum_{m=0}^{M-1} w_m f(\mathbf{r}, t - \Delta_m) \quad , \qquad [1]$$

where $z(\mathbf{r},t)$ is the focused sound field, w_m is a weighting factor, $f(\mathbf{r},t)$ is the sound field from a single sensor, and Δ_m is a time delay(Yu et al. (29)). The sound field from a single sensor is determined by the particular guided-wave mode and frequency that is being used for the inspection. For focusing at an arbitrary location, the individual array sensors must have some multi-directional properties. For this reason, several novel omni-direction EMAT sensor designs were considered in this work.

For a practical ILI implementation, the sensors should not require any type of coupling liquid and should be capable of efficiently generating CLT-waves in the pipe wall. EMATs were determined to be the most appropriate sensor type as they generate and receive ultrasound by coupling magnetic fields to the flow of current within a specimen. EMATs can be non-contact, operate at elevated temperatures, work on rough or oxidized surfaces, and operate at high speeds. Depending on the configuration of the magnetic field and eddy currents, Lamb and shear horizontal guided waves can be both generated and received.

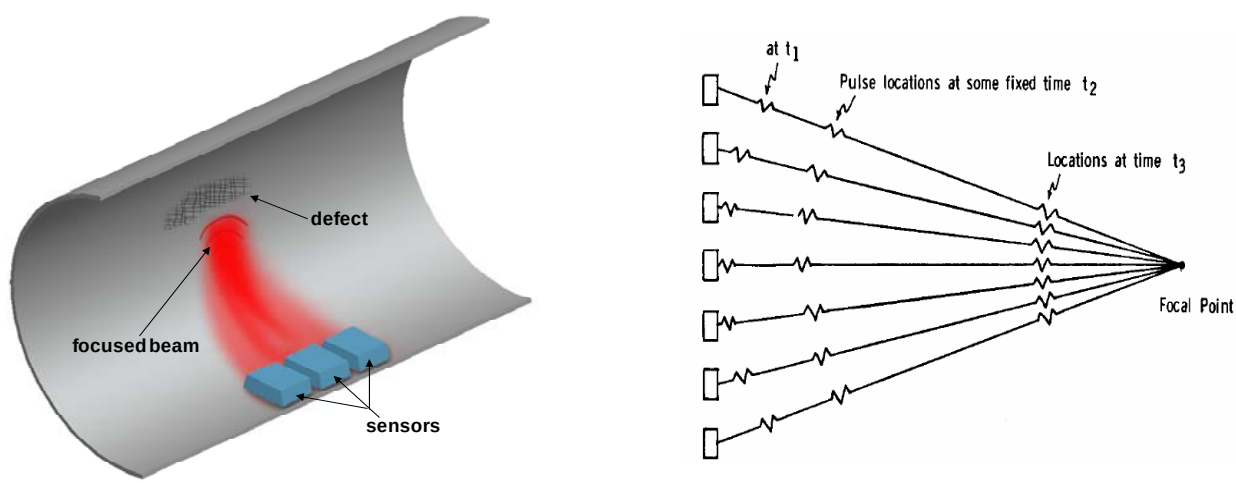

Figure 3.1. Guided wave phased array concept for ILI using EMATs.

The EMATs used in this project are Lorentz force EMATs. Figure 3.2 illustrates the Lorentz concept. The first component to the Lorentz force transduction mechanism is an eddy current. An eddy current (*J*) is induced in the part by passing a current (*I*) through a wire or trace in close proximity to the specimen. The part to be inspected must be conductive for this to occur. In addition to the eddy current, a static magnetic field (*B*) must be present. When the current is pulsed in the presence of the magnetic field a force (*F*) is induced in the specimen. The direction of the force can be determined by the right hand rule. The magnitude and direction of the force are given by Equation 2, where *F* is the force per unit volume, *J* is the induced dynamic current density, and *B* is the static magnetic induction.

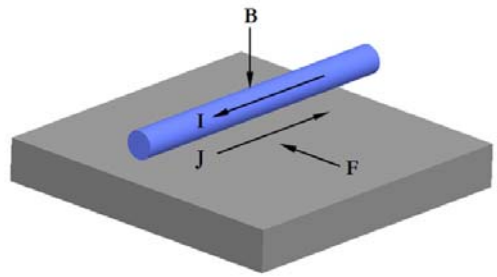

Figure 3.2. Lorentz EMAT transducer principle.

$$F = J \times B \qquad [2]$$

The two most typical Lorentz force EMATs configurations are for the generation of Lamb and SH waves. Figure 3.3 shows the configuration of a Lamb wave EMAT. Lamb wave EMATs generally use what is referred to as a meandering coil with a single large magnet. The wavelength of the induced wave can be altered by changing the spacing between the traces in the coil. For both the Lamb wave and SH wave EMATs, changing the wavelength of the sensor allows the designer to sweep through the dispersion curve space. A given wavelength activates a line on the dispersion curve that originates at the origin, with a given slope. The slope of the line can be altered by changing the spacing. A specific mode, or modes, can then be activated by exciting the transducer at a set frequency.

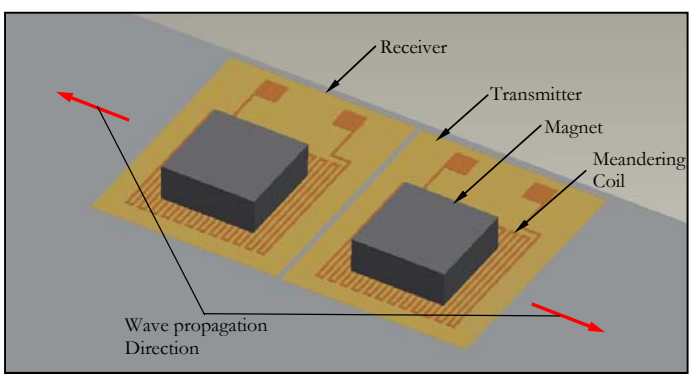

Figure 3.3. Lamb wave EMAT transducer.

Three different EMAT coil configurations were designed and fabricated. Because the focus at the time was on a 24-*in* schedule 40 pipe, all three coils were designed to generate a 200 *kHz* A0 or 456 *kHz* S1 Lamb-type wave in a 0.25-*in*-thick pipe. The coils were made by etching coil patterns out of a 0.01-*in*-thick copper layer on a 0.015-*in*-thick PCB substrate. These specifications were chosen such that the coils would be able to support high current excitation

without arcing. Lamb-type waves are then generated by placing a large permanent magnet over the coils. The interaction of the magnetic field with the eddy currents created in the pipe wall will manifest in a propagating elastic wave. Permanent magnets designed to match the different coil geometries have also been acquired.

As shown in Figure 3.4(a), one coil design is directionally focused. The fixed focal point is at approximately 19 *in* from the sensor. Several sensors of this geometry will be used to focus energy at the same location for enhanced sensitivity. They will be used specifically for exploring the potential of geometric focusing in the circumferential direction of pipe. The geometries seen in Figure 3.4(b) and (c) were designed for omni-directional excitation, or equal excitation in all directions. An advantage of this geometry is that it can be used for either geometric focusing or real-time phased array focusing. By using a phased array, a focal point can be created at any desired point in the structure through the use of the appropriate time delays. The same omni-directional sensors can also be positioned in a geometric pattern so to achieve geometric focusing. The coils shown in Figure 3.4(b) and (c) are different ways of achieving the same outcome and the results from directionality tests are compared here to determine the optimal design for generating omni-directional waves.

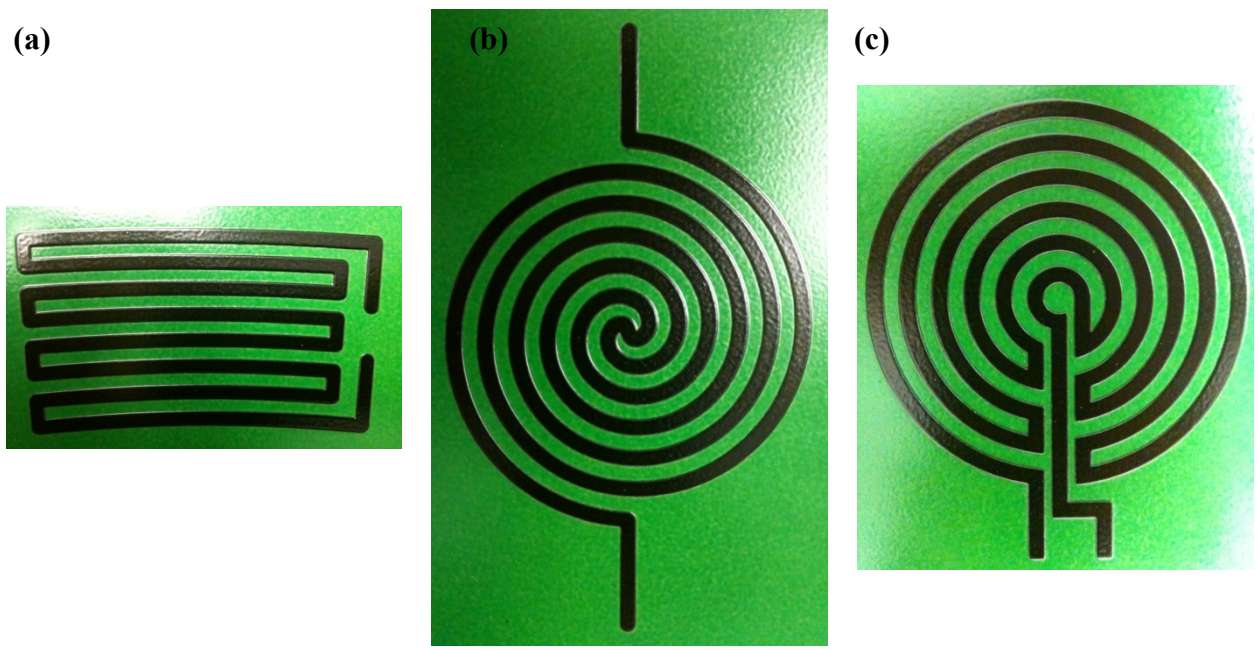

Figure 3.4. EMAT coil configurations fabricated for laboratory testing, including (a) directionally focused coils and omni-directional (b) spiral coils and (c) labyrinth coils.

An experiment was designed, using a 0.25-*in*-thick steel plate, to test the directionality properties of the circular coils. In the experiment, the receiving coils remained fixed and the transmitting coil was spun in a 360° circle, as illustrated in Figure 3.5. Excitation was done with an arbitrary waveform generator and a 1200V-gated amplifier. A six-cycle rectangularly windowed toneburst was used for the directionality tests. The optimal excitation frequency was found to be approximately 175 kHz for the circular coils. A wave velocity measurement of the directly transmitted pulse was completed and it was determined that the dominant wave packet had a group velocity of approximately 3.1 mm/µs. This agrees well with the group velocity of the A0

mode at the same frequency as determined from the theoretical group velocity dispersion curves. It is therefore concluded that the coils successfully generate the intended mode near the designed frequency of 200 kHz. In Figure 3.5, a 3-*in* diameter, 0.5-*in*-thick NdFeB permanent magnet is used to generate the necessary magnetic fields.

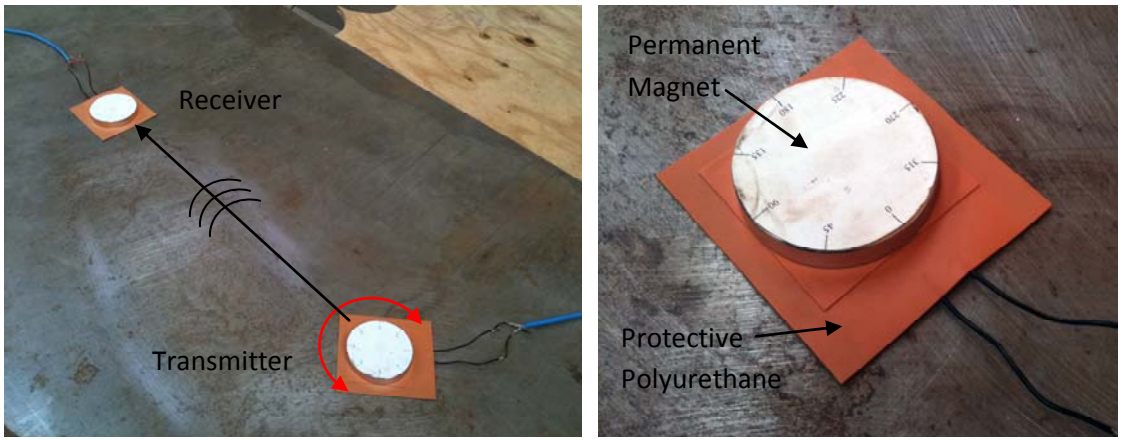

Figure 3.5. Photographs showing experimental setup for omni-directional coil directionality tests. The transmitting coil was rotated 360° while the receiver remained fixed in place.

The results of the directionality tests can be seen in Figure 3.6. It is seen in both plots that the circular coils successfully generated waves in all directions though not with equal efficiency. In the case of the labyrinth coil, Figure 3.6(b), this can be understood by noticing that excitation is impeded in the direction coinciding with the coil leads and turning points (straight sections). Because the eddy-currents produced in these regions of the coil are not in the circumferential direction, it is not unexpected that a wave is not efficiently generated in this direction. At this time, it is not fully understood why the spiral coil design has a preferred excitation direction but it is most likely related to direction of the eddy currents produced by the coil leads. This problem can be easily fixed in the future by not etching the leads directly on the PCB.

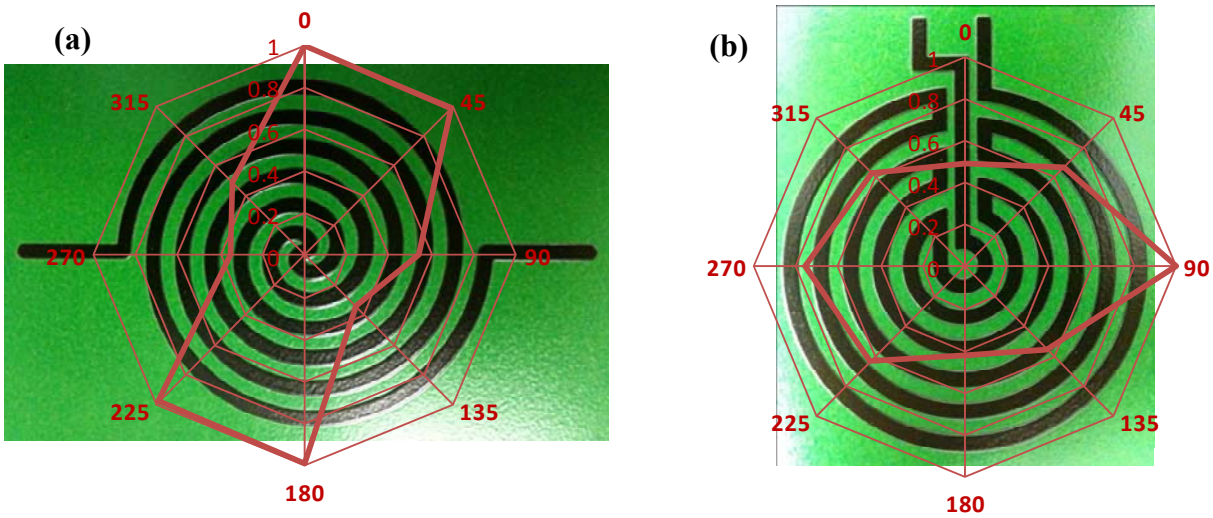

Figure 3.6. Polar plots showing directionality properties of the omni-directional (a) spiral coils and (b) labyrinth coils. It is seen that both coils favor excitation in particular directions.

Figure 3.7 shows a photograph of the focused coil EMAT with a 2 x 3 x 0.5 *in* NdFeB permanent magnet to produce the necessary magnetic field. Several layers of polyurethane sheeting were used to protect the coils from the magnet and a thin layer of ultra-high molecular weight (UHMW) polyethylene was used as an abrasion resistant layer between the coil and the steel plate. The focused coil was found to be optimally excited using a 200 kHz 3-cycle pulse. This agrees perfectly with the design specifications. Figure 3.8 shows a comparison of the RF waveforms received from each of the three different types of coils. It is seen that the result in Figure 3.8(c) from the focused coil has a far superior signal-to-noise ratio as compared to that of the (a) spiral coil and (b) labyrinth coil. This is expected as the circular coils send the same amount of energy in many directions that the focused coils concentrate along a single line. From this result, it appears as though the focused coil is perhaps the best option for a geometrically focused array.

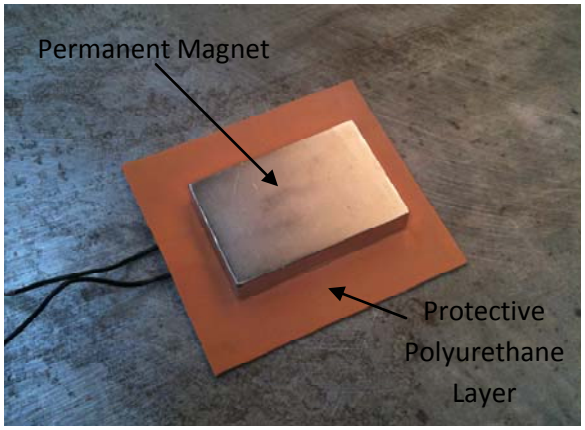

Figure 3.7. Photograph showing the focused coil EMAT.

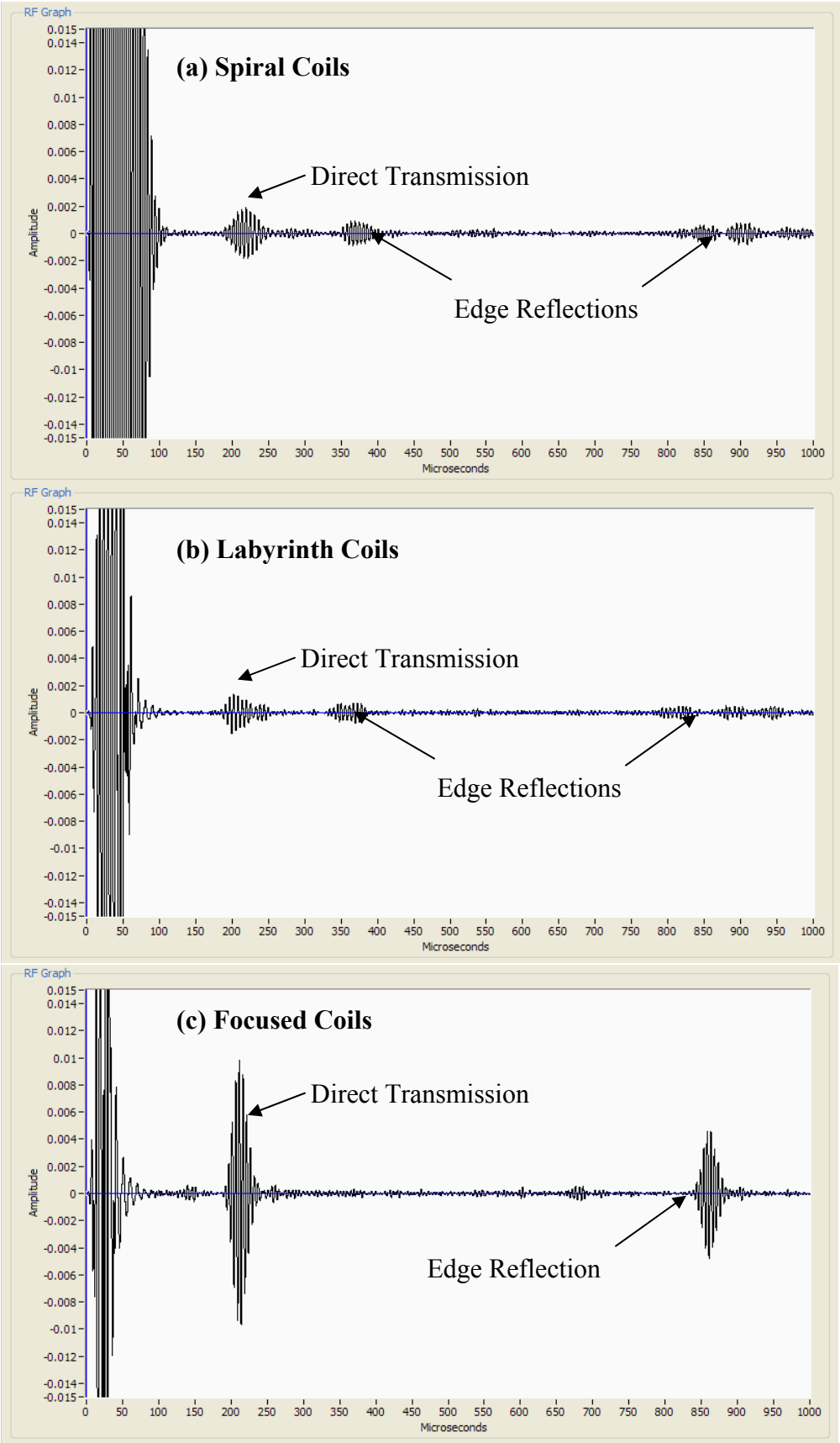

Figure 3.8. RF waveforms obtained using the different types of coils. It is seen that the (c) focused coils produced the best signal-to-noise ratio. The much weaker signals obtained from the (a) spiral and (b) labyrinth coils is expected as the energy is being transmitted in many directions as opposed to along a single line.

(ALL RESULTS ARE PLOTTED ON THE SAME SCALE)

Another topic that must be considered when selecting a focusing implementation for an ILI tool is the rate at which data can be acquired. While data acquisition speeds and file sizes are not typically of concern in most NDE applications, they are critical factors in the development of a practical ILI tool. If data cannot be acquired quickly enough, or if the data volume exceeds the memory reserves of the autonomous tool, the inspection will be ineffective. The following paragraphs discuss in detail the expected acquisition speeds and file sizes of a guided-wave ILI tool. Several different tools and hardware configurations are considered.

As previously discussed, the excitation frequencies for the proposed application are 200 *kHz* to 456 *kHz*. At these frequencies, the optimal sampling rate is approximately 5 *MHz*; however, due to the EMAT's susceptibility to high-frequency electromagnetic noise, it is often necessary to sample at 25 *MHz* if hardware filters are not being used. This is because the high-frequency noise must be sampled correctly for it to be removed properly. If hardware filters are used to remove the high-frequency noise, the sampling rate can be dropped to 5 *MHz*, decreasing the number of acquired data points by a factor of five, effectively decreasing file sizes by a similar factor. Table 3.1 shows the effect on file size of different acquisition settings and hardware capabilities that have potential to work with the application being studied. It is seen that there is a linear relationship between acquisition length and file size.

Table 3.1. Breakdown of saved waveform file sizes with different parameters. All data in files have a precision of 3.

Frequency (KHz)	Hardware Filter (Low-pass) (KHz)	Hardware Filter (High-pass) (KHz)	Acquisition Length (µs)	Sampling Rate (MHz)	File Size (1 Receiver) (KB)	File Size (2 Receivers) (KB)
100-500	None	None	1000	25	183	344
100-500	None	None	500	25	92	172
100-500	500-1000	0-250	1000	5	37	69
100-500	500-1000	0-250	500	5	19	35

The use of synthetic focusing was considered as a means of focusing at any location in the pipe via the post processing of *n(n-1)* signals, where *n* is the number of sensors in the array. In synthetic focusing, one sensor is used as a transmitter and the remaining sensors as receivers. Once data is acquired with one transmitting/receiving combination, the next sensor in the array is used as a transmitter until all sensors have been used. For example, if three transducers are used for synthetic focusing a total of three iterations will have to be run. There will be one transducer transmitting the signal and two transducers receiving. The transmitting and receiving transducers will change with every iteration, as shown in Table 3.2. The question is raised as to whether the six signals (for a three-sensor array) can be acquired and stored before the tool has moved a considerable distance. Using an absolute minimum group velocity of 1.5 mm/µs and a focal point of approximately 18 *in*, the time for the transmitted wave to travel to the focal region

and back, given a possible reflector, is 643.5 μs. Therefore, with three iterations it will take at least 1.930 *ms* for all three waveforms to be transmitted and received. However, the data acquisition program also adds acquisition time as the transmitting/receiving electronics must be reconfigured at each iteration. Also, triggers need to be generated and the data acquired needs to be downloaded from the DAQ card's onboard memory.

Table 3.2. Transmitting and receiving setup for synthetic focusing.

Transmitter	Receiver
1	2&3
2	1&3
3	1&2

The time needed to configure the electronics, generate triggers, and download the data counters was estimated for two different system configurations. The first system used was a pulser/receiver card, DAQ card, and switching-card system. The program for which the time estimates were extracted is similar to that which would be used in a synthetic phased-array system. With the counters in place, it was shown that a single iteration takes about 0.3 seconds, resulting in a total of approximately 0.9 seconds to acquire all necessary data. This is an estimate as the actual value could only be obtained by assembling and testing the electronics.

For real-time phased array focusing, all array sensors are used for excitation. Time delays are added to each sensor to focus the waves at a predetermined focal region. For receiving, either one or all of the array sensors may be used or an entirely separate sensor may be used. By employing counters in an actual real-time phased-array system, it was found that the time to focus at one point with the real-time phased-array system is relatively quick, taking only 1 *ms*. The process is expeditious because there is no switching of channels, enabling all tasks to be completed in a single iteration. Though much quicker than synthetic focusing, real-time focusing acquires information at only one focal point, whereas the data acquired for synthetic focusing can be used to focus at all possible points via post-processing. The data acquisition rates are summarized in Table 3.3.

A third type of phased array is a geometric phased array, in which the time delays are physically built into the array geometry. For example, the array sensors may be placed around a portion of a circle so to focus the waves at the center of the circle. Figure 3.9 shows an example of a geometrically focused array in which the sensors have been mechanically phased to focus energy at a distance of approximately 19 *in*. Different geometric arrays can be designed to focus at any point within the range of the array. In this way, all sensors are excited simultaneously and either one or all of the array sensors can be used as receivers, or an entirely separate sensor may be used as a receiver. Again, because there is no switching of channels, all necessary tasks can be completed within a single iteration, making the process fast. A major advantage of the geometric array is that requires significantly less electronics, making the system cheaper and smaller. One

disadvantage is that the focal point is fixed so a critical zone would have to be identified as the focal point, such as the bottom of the pipe since this is where corrosion often occurs.

Table 3.3. Data acquisition times for various phased-array systems.

	Total Channels	Time for 1 Iteration	Total time for acquisition
Synthetic Phased Array	3	0.3 s	0.9 s
Real-Time Phased Array	3	1 ms	1 ms
Geometric Phased Array	1	1 ms	1 ms

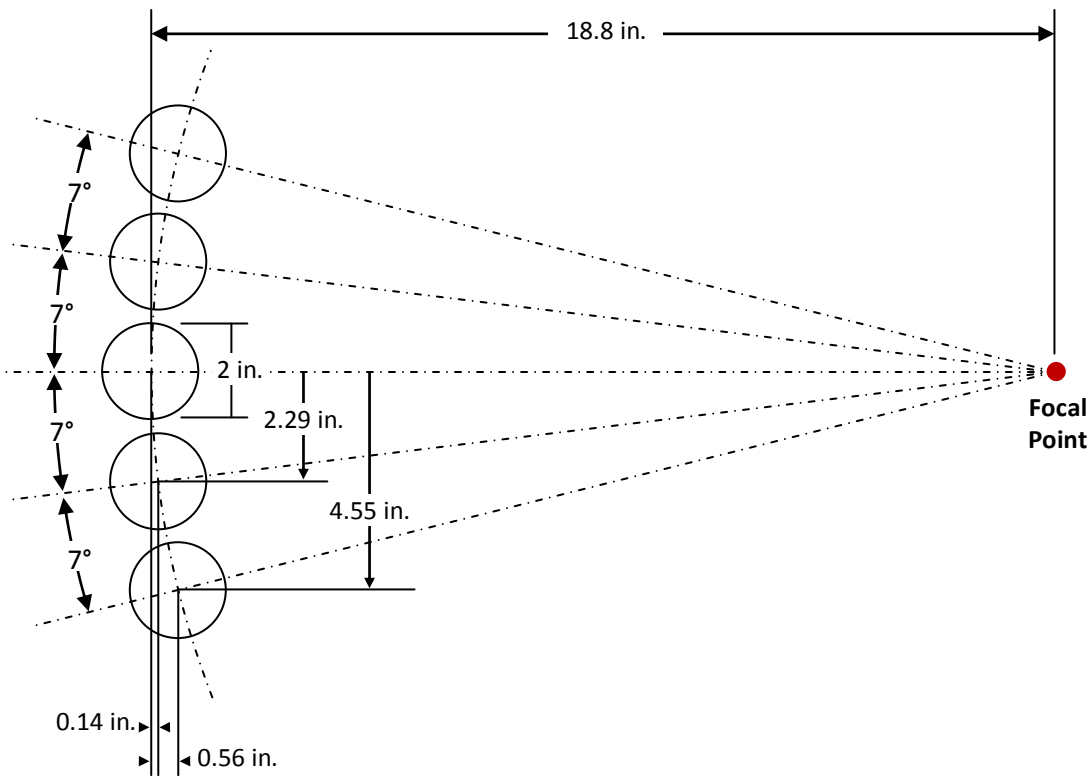

Figure 3.9. Geometrically focused array concept showing how mechanical phasing of the individual array sensors can be used to form a focal point at a specific location.

Because the cost of the electronics required to build a real-time phased array for an ILI tool was beyond the scope of this project, it was decided that the geometrically focused array was the most viable approach to demonstrating the benefits of the focusing concept. In the future, similar results could be achieved using time-delayed phasing rather than the mechanical phasing

used in a geometric array. Furthermore, it was decided the geometric array would be used to focus energy at the bottom of the pipe, as this is a hot spot for corrosion.

The next section of this report discusses the results of numerical models that were created to verify the focusing concept and to identify potential features that could be used to provide sizing information for a corrosion anomaly.

4. NUMERICAL MODELING OF CIRCUMFERENTIAL GUIDED WAVES

Numerical modeling is a very powerful technique that can be used to verify analytical results or to solve problems that are too complex to have closed-form analytical solutions. Effectively, finite-element modeling is a quick and cost effective virtual experiment that has the added benefit of being free of experimental error. In this work, numerical modeling was used to demonstrate the applicablility of the mode/frequency combinations identified in the previous section to corrosion defect sizing using the focused array method and to identify potential sizing features. Two primary defect geometries were determined to be of primary interest: long and narrow corrosion, and small pitting anomalies. Sizing using MFL technology for these types of defects has a high tolerance and low certainty.

To study the focusing concept numerically, several different EMAT coil configurations were investigated. These configurations can be seen in Figure 4.1 and include a traditional straight-trace coil, a focused coil, and a focused array of coils. To compare the response from the different sensor configurations (i.e. straight, curved, and focused array) a numerical model was created in which a 0.243 *in* thick steel plate contained a 1 *in* long, 0.25 *in* wide, and 50% through wall corrosion patch. A plate was used in place of a pipe due to computational limitations, though the dispersion curves for the two different structures are similar. Figure 4.1 shows the modeled sensor geometry, a still frame showing the energy reflected from the defect, and the analytic envelope of the reflected energy. In each of the analytic envelopes it is seen that amplitude of A0 defect reflection, relative to the A0 backwall reflection, is improved by using curved coils and furthermore if the curved coils are arranged in a focused array. Additionally, the relative amplitude of the S0 mode conversion from the backwall decreases significantly by using the focused array.

Figure 4.2 summarizes the results from the modeling comparison of the different sensor configurations. It is seen that by using a focused coil array, the amplitude of the defect reflection is improved by 6dB relative to the amplitude of the unwanted mode conversion. Furthermore, by using a focused coil array, the amplitude of the defect reflection is improved by 9dB relative to the amplitude of the backwall, i.e. the defect reflection is only 3dB smaller than the backwall reflection. This is a significant improvement in signal to noise ratio.

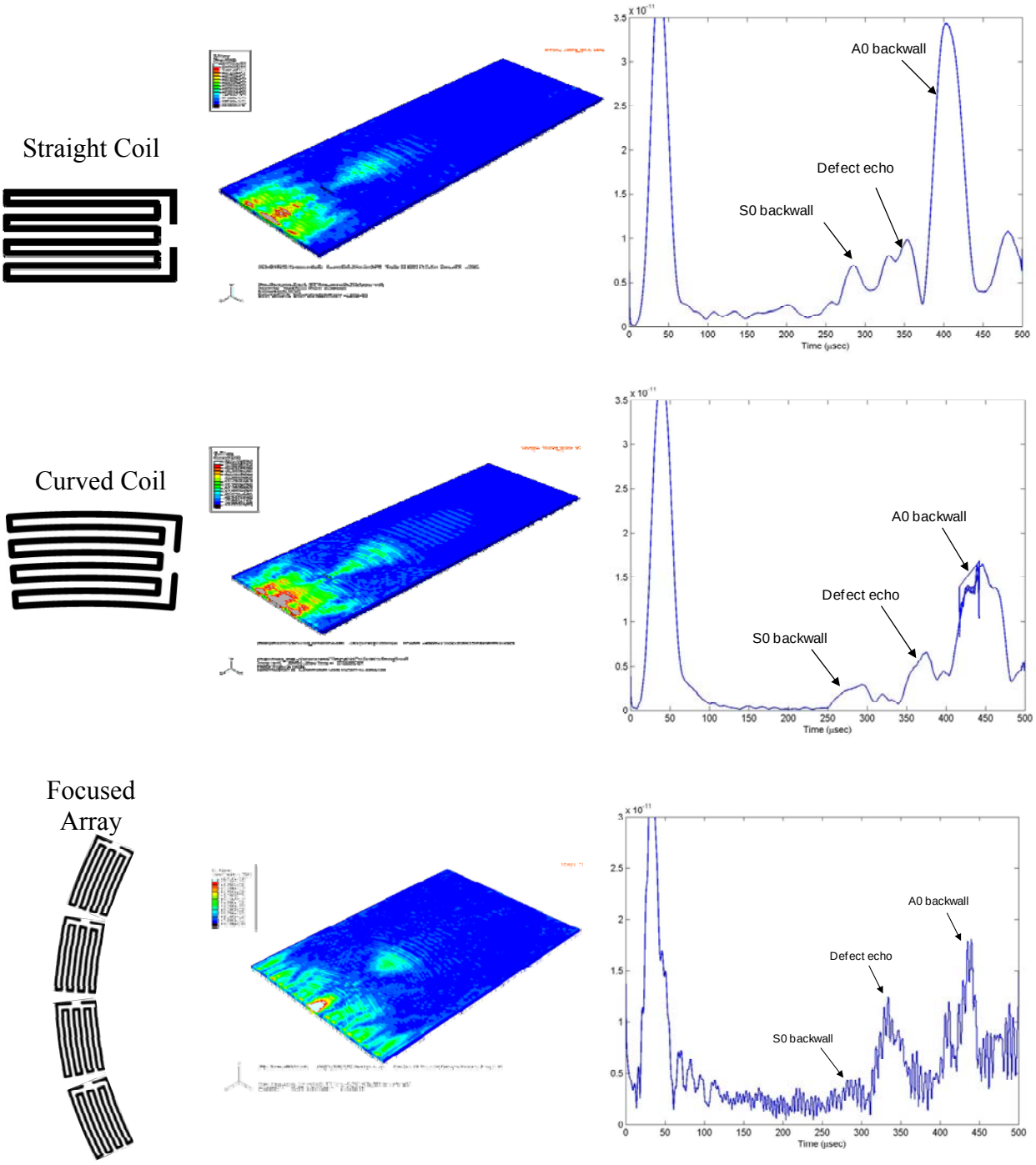

Figure 4.1. RF-waveform envelopes showing the decrease in signal amplitude as EMAT sensors are removed from the focused array.

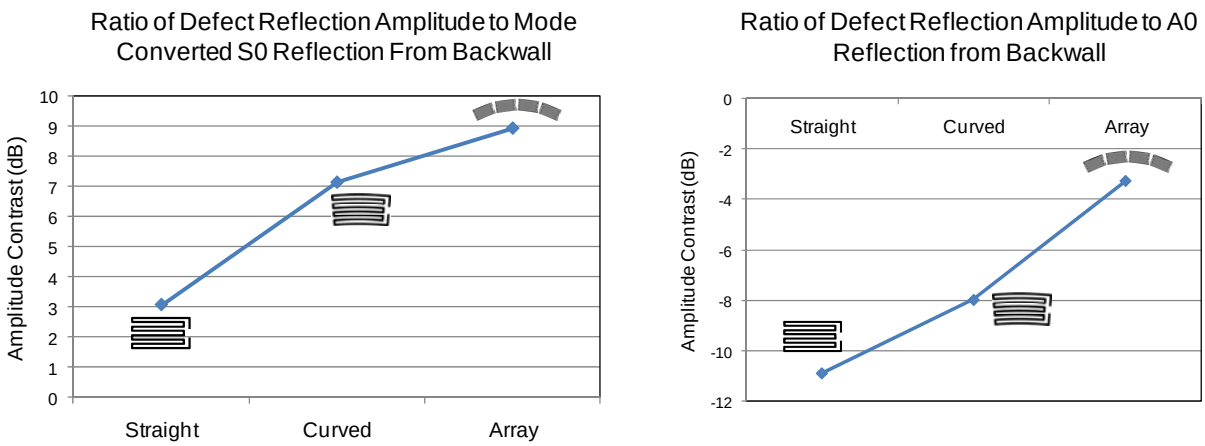

Figure 4.2. Summary of results from modeling comparison of the straight, curved, and curved array sensor configurations.

Another significant advantage of the focusing approach is the ability to obtain improved lateral resolution. This is illustrated in Figure 4.3 and Figure 4.4 using the 200 *kHz* A0 mode. A numerical model wave created with receiving nodes across the entire width of the plate at 17 axial locations, as shown on the top in Figure 4.3. A 0.375 *in*-thick steel plate was used to approximate a 12 *in* schedule 40 X52 steel pipe. The focal distance was designed to be at approximately 9.5 *in* as this corresponds to one quarter of the circumference of the pipe. It is seen that the focused array produces a highly concentrated energy packet at the focal point (Figure 4.3, bottom). Figure 4.4 shows a 3D plot (top) of the wave amplitude across the width and length of the plate near the focal zone. The bottom plot of Figure 4.4 shows the amplitude profile across the plate at the focal line. It is seen that the 6 dB beam width is approximately 0.5 *in* which is much smaller than that of a single straight trace coil. For the single straight trace coil, the beam width at the same point would be at least as wide as the sensor (~ 3 *in*) or wider due to beam spreading.

So the ability to use a geometrically focused array has been verified via numerical finite-element modeling and the benefits of such an array include increased signal-to-noise ratio at the focal point, a reduction in coherent noise, and improved lateral resolution. Another key benefit that has not been demonstrated here but has been well documented for phased array focusing of long-range pipe inspection tools is the improved penetration power in coated pipe using the focusing approach.

Numerical modeling was also used to investigate the interaction of the 456 *kHz* S1 guided wave mode with small pit-like corrosion defects. A numerical model was designed, as shown in Figure 4.5, in which a 1 *in* diameter circle was used to create elliptically shaped pitting defects on the inside surface a 12 *in* schedule 40 X52 steel pipe. The damage states were varied from 0% to 100% through-wall depth at the deepest point of the pit-like defect. EMAT loading was incorporated and two receiving nodes were placed so to received both reflected and transmitted energy from the defect. A still frame from an animation showing the wave being reflected and transmitted by a 60% through-wall defect is shown in Figure 4.6.

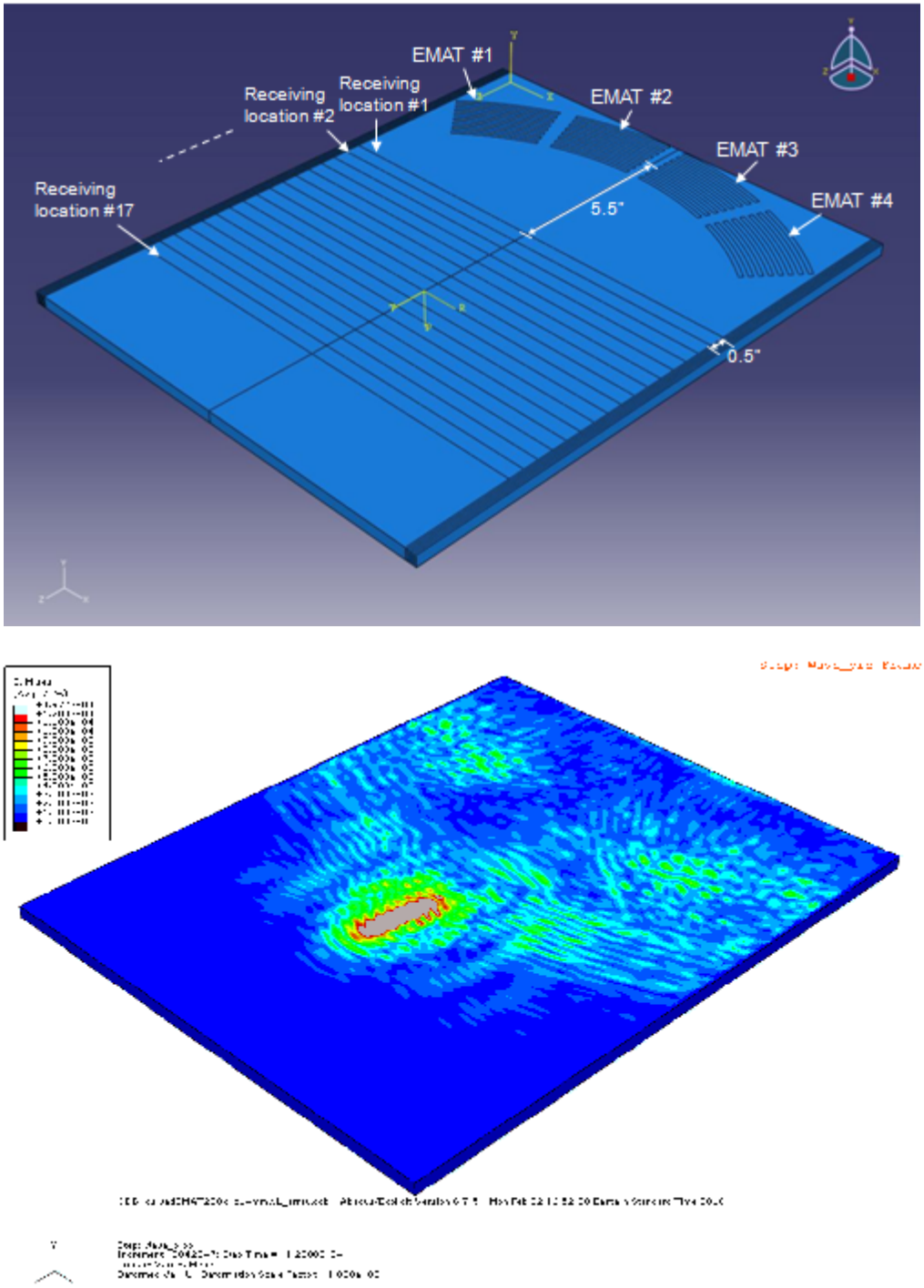

Figure 4.3. Image showing model configuration (top) for studying the width of the focused beam profile at the focal point. The result shown on the bottom shows a highly concentrated beam at the focal point.

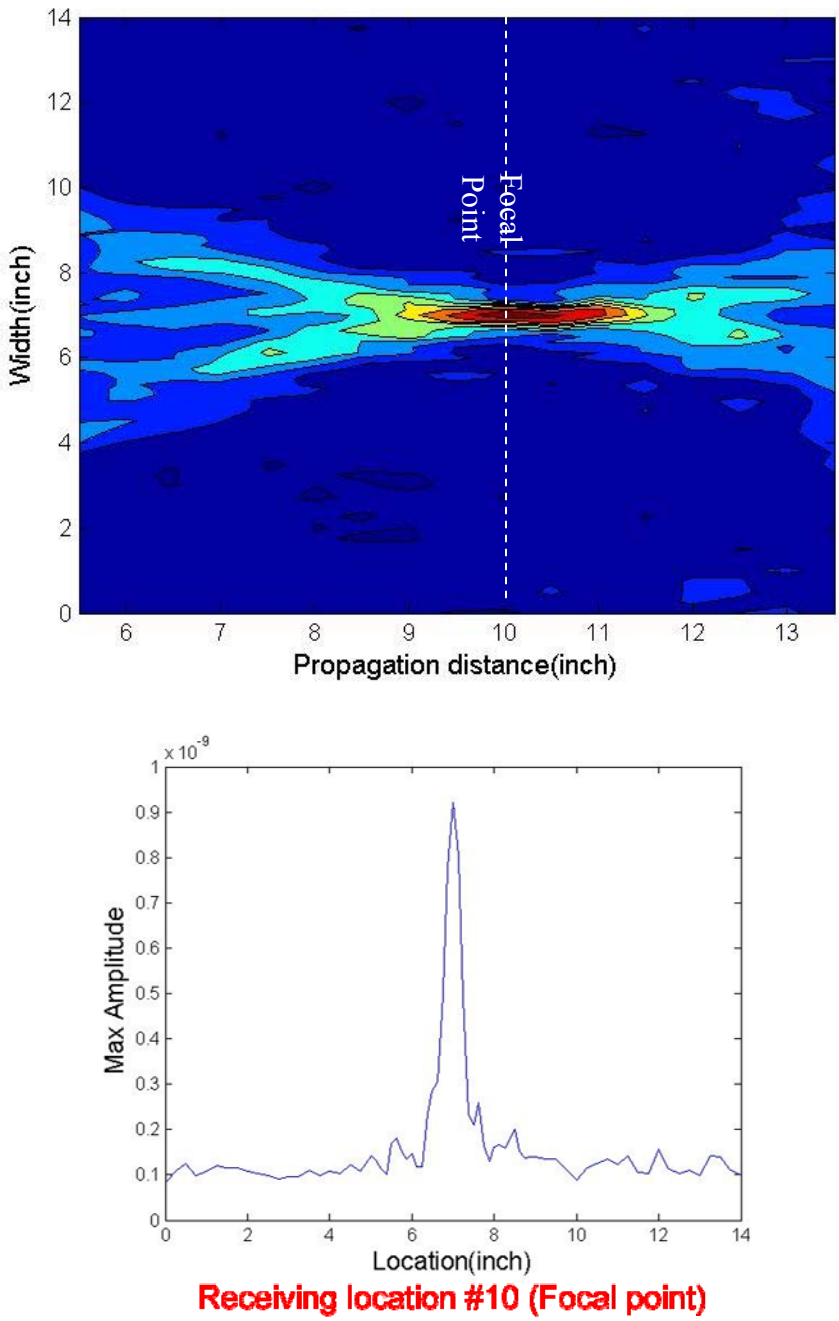

Figure 4.4. Plot of wave amplitude across the width of the plate model shown in Figure 4.3. It is seen that the 6 dB beam width is approximately 1 *in*.

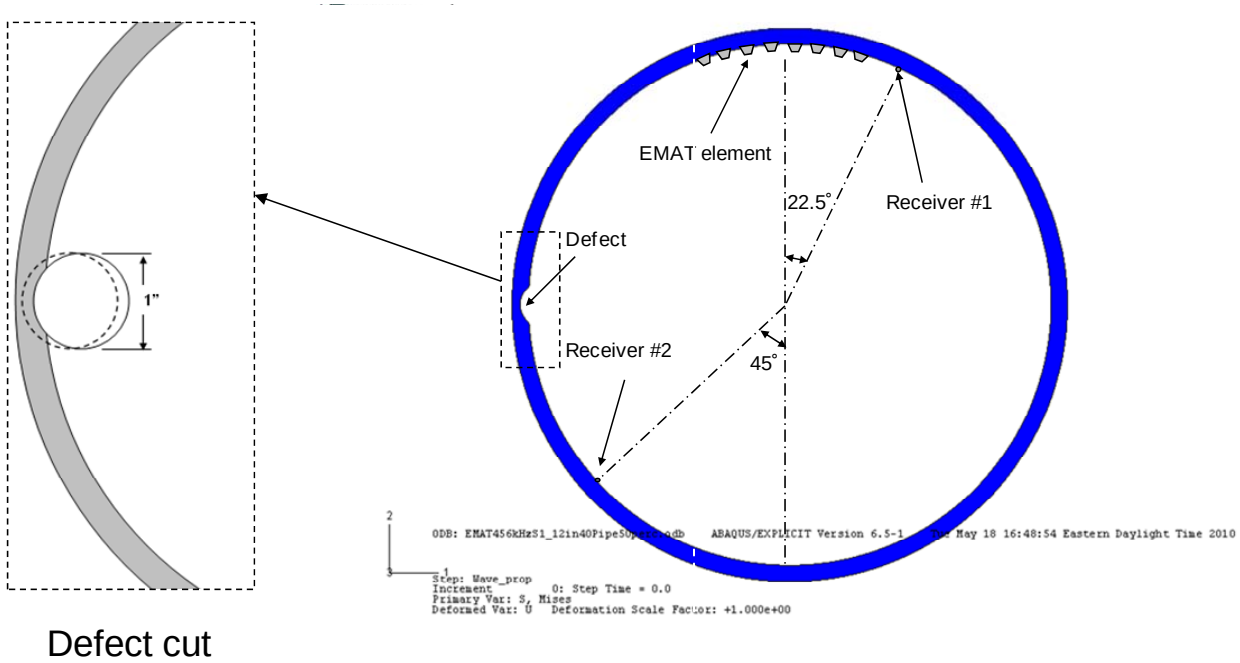

Figure 4.5. A 456kHz S1 guided wave is generated in the circumferential direction in a 12 *in* schedule 40 X52 steel pipe by an EMAT. 0%~100% through-wall spherical defects are cut on the inner surface of the pipe as shown on the left.

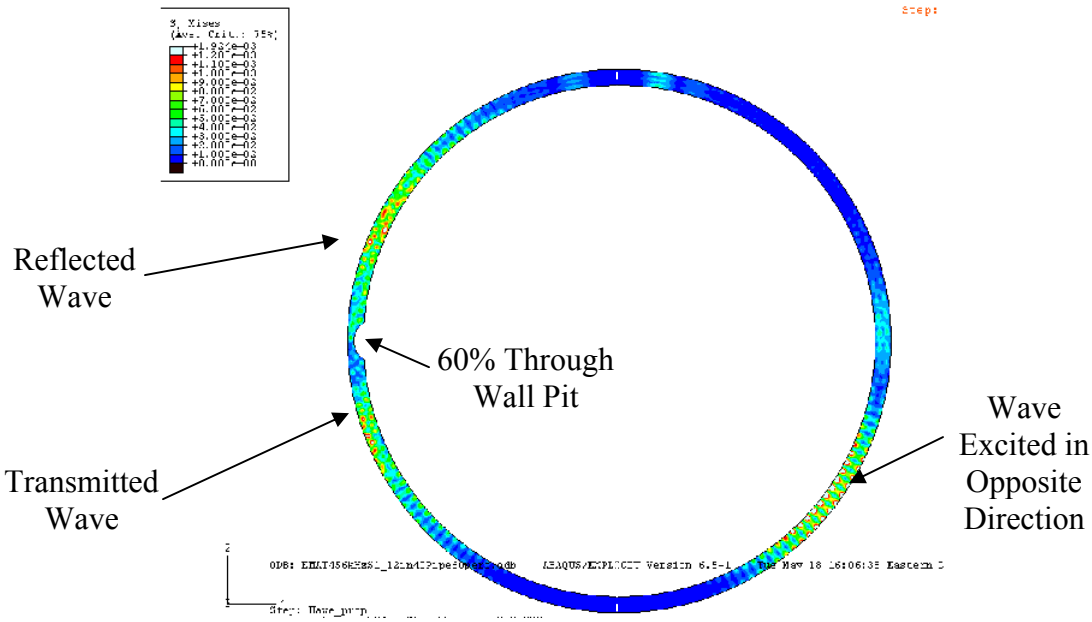

Figure 4.6. Still frame from animations showing 456 *kHz* S1 mode being transmitted and reflected by a 60% through-wall pit-like defect.

Figure 4.7 shows the analytic wave envelopes for several of the defects states described in Figure 4.5. Both reflected and transmitted waveforms are shown for the 456 *kHz* S1 mode and it is seen that as the through-wall depth of the defect is increased, the amount of reflected energy increases, and the amount of transmitted energy decreases. It is also seen from Figure 4.7 that the sensor arrangement used in the numerical model allows for the easy identification of the reflected and transmitted S1 mode as it has the fastest group velocity of any of the potentially propagating modes. Furthermore, from Figure 4.8 it was seen that these trends correlated well to the depth of the pit-like anomalies and will therefore serve as a good sizing feature.

In a real inspection environment, raw amplitude is a difficult feature to analyze because it can be affected by sensor liftoff, attenuation, etc. To use amplitude information in a more reliable fashion, it can be normalized against another pulse that has been generated by the same sensor, such as the directly received backward propagating pulse or latent backward propagating pulse shown in Figure 4.7. This will be demonstrated experimentally in the next section.

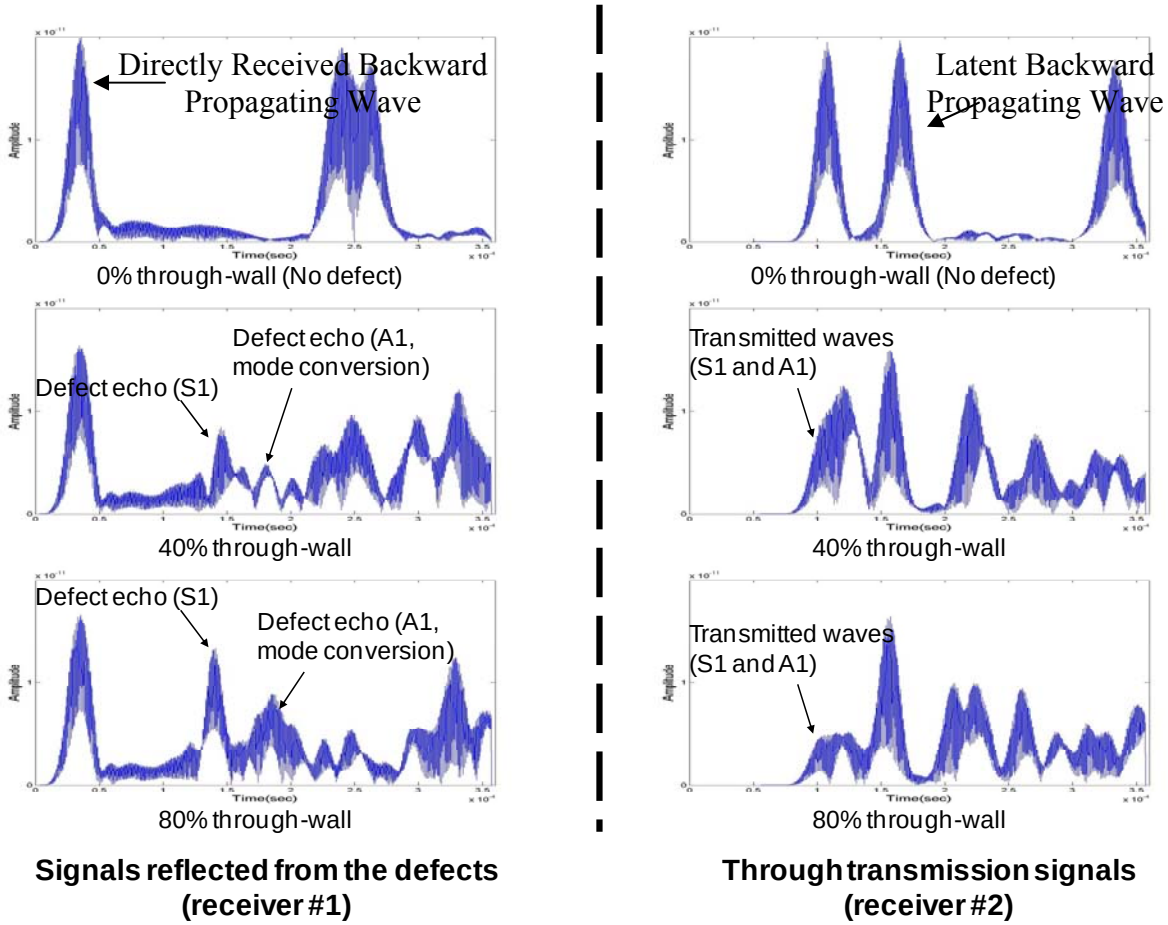

Figure 4.7. Analytic wave envelopes of the reflected (left) and transmitted (right) 456 *kHz* S1 wave mode for pipe with no defects (top), with a 40% through-wall pit (middle), and with an 80% through-wall pit (bottom).

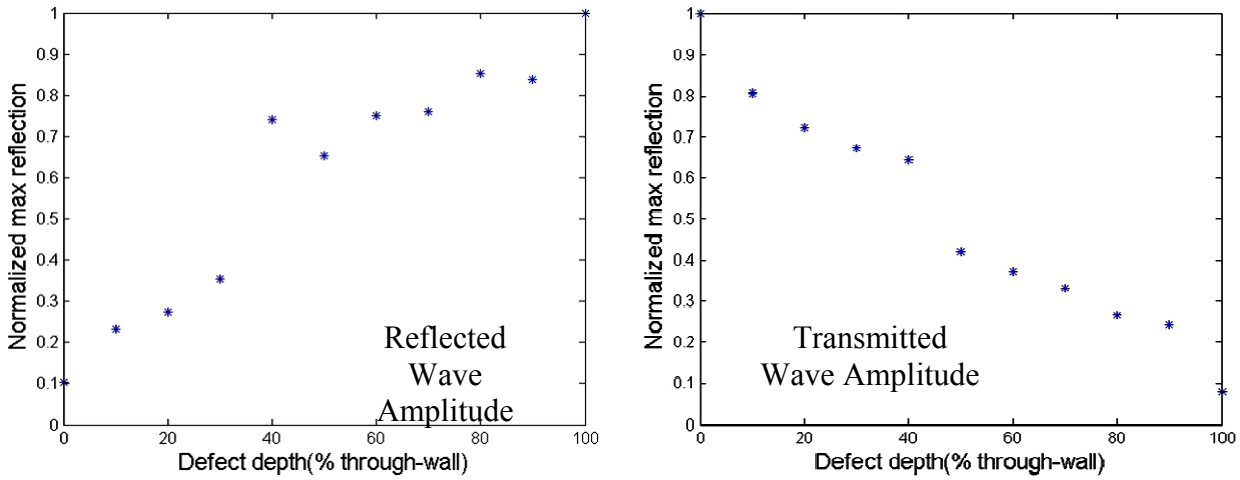

Figure 4.8. Plots comparing reflected (left) and transmitted (right) signal amplitude for a 456 *kHz* S1 wave impinging upon a pit-like defect with 0% to 100% through-wall depth.

It has been demonstrated through numerical finite-element modeling that geometric focusing can be used to improve defect detection and sizing capabilities of MFL tools. Furthermore, it was shown that both the reflected and transmitted wave amplitude of the 456 *kHz* S1 mode can be correlated to the depth of a small pit-like defect. The next section will concentrate on the experimental verification of these concepts.

5. EXPERIMENTAL PROOF OF CONCEPT

In this section, the results of the analytical and numerical modeling are verified experimentally. The benefit of a geometrically focused array is demonstrated experimentally and multiple sizing experiments are performed using a prototype ILI tool that was built for this purpose. Two primary test specimens were used: a 12 *in* diameter schedule 40 X52 steel pipe with machine made defects and a similar pipe sample that had been removed from service because of naturally occurring pitting. The equipment and ILI tools used for data acquisition are also described.

The experiment shown in Figure 5.1 demonstrates that using a geometrical focusing technique with EMATs greatly improves signal-to-noise ratio compared to single transducer excitation. To demonstrate the benefits of focusing, three experiments were performed with different transmitter alignments on a 0.25 *in*-thick steel plate. This experiment was originally performed under the assumption that the final application was going to be for a 24 *in* schedule 40 pipe. Though the final application was eventually switched to a 12 *in* diameter pipe, the results from this experiment are still relevant and demonstrate that a geometrically focused array can provide significant benefits over a single transmitting element. It should also be noted that for larger diameter pipe, the dispersion curves are sufficiently similar to that of a plate of the same thickness.

For all experiments the transducers were pulsed at 1200 volts at a frequency of 200 kHz. The transmitters are aligned to focus at 19 *in* from the array radius. To measure the signal amplitude, a receiving EMAT was placed at 19 *in*. Photographs of the experimental setup and of the corresponding RF waveforms can be seen in Figure 5.1. First a reference signal was obtained from the direct transmission of one transmitter at 19 *in* (Figure 5.1(a)). The amplitude of this wave was 2.89 mV. The second experiment configuration consisted of two transmitters that were aligned to focus at 19 *in* as shown in Figure 5.1(b). A wave amplitude of 3.278 mV was recorded. This is a 3.12 dB increase from the reference signal. For the third experiment a three transmitter configuration, as shown in Figure 5.1(c), was used. An amplitude of 4.177 mV was obtained, which is a 5.22 dB increase from the reference signal. The experimental results are summarized in Table 5.1.

To show that the array was actually focusing at a distance of 19 *in*, the receiving transducer was moved to a distance of 22 *in*, 3 *in* beyond the focal point. The corresponding RF waveform is shown in Figure 5.22. An amplitude of 1.3 mV was obtained, which corresponds to a 10.14 dB decrease when compared to the three EMAT focused array. The receiving EMAT was also moved 3 *in* in front of the focal zone and a 2.06 dB decrease in signal amplitude was obtained; further confirming that the array was focusing at the proper location. This result is quite significant as it shows that it is possible to nearly double the signal-to-noise ratio without increasing the pulsing power by using the geometrical focusing technique.

Table 5.1. Summary of results from geometrical focusing experiments

Number of Transducers	Voltage (mV)	Gain (dB)
1	2.289	-
2	3.278	+ 3.12
3	4.177	+ 5.22

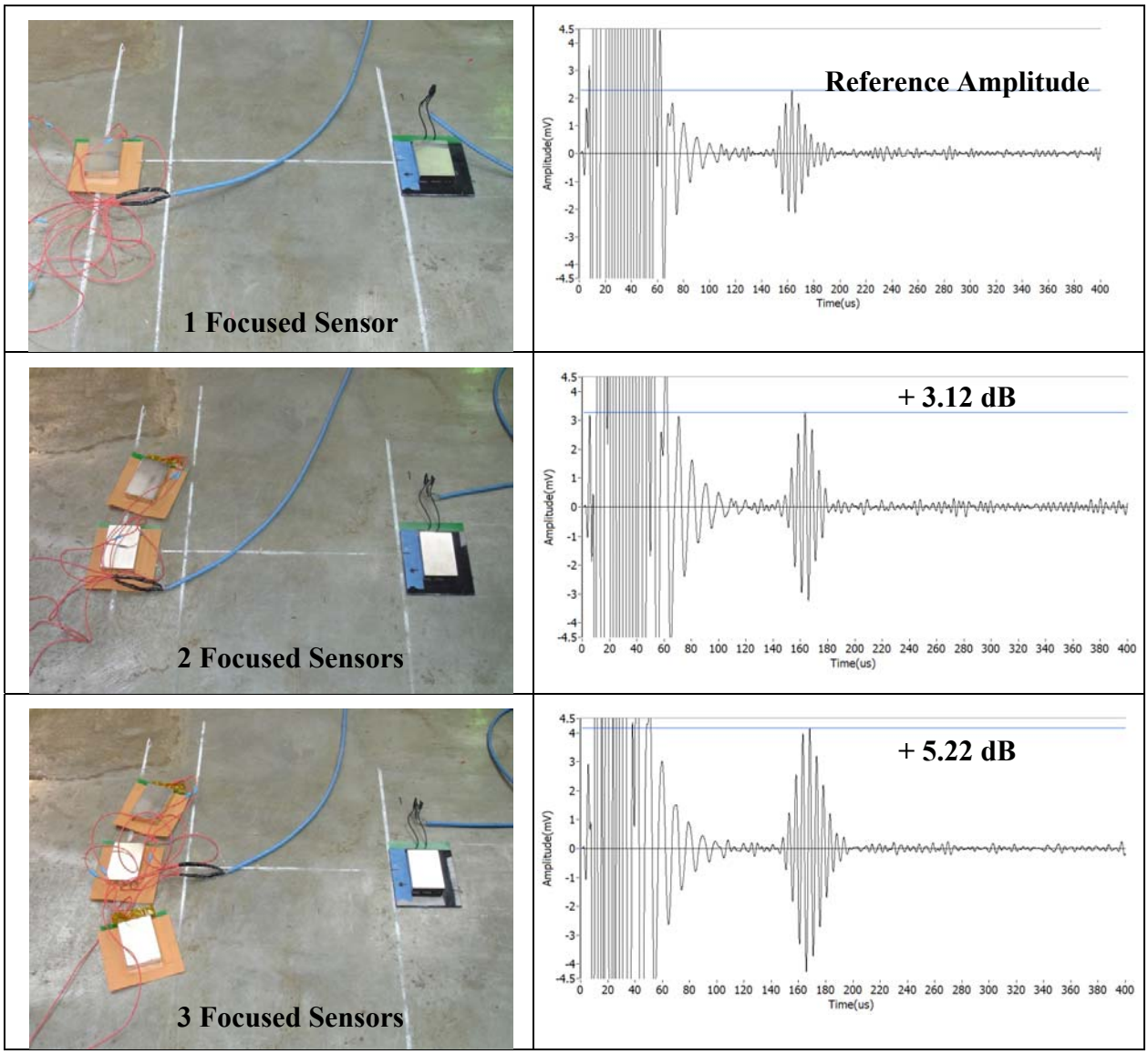

Figure 5.1. Photographs of experimental setup and corresponding acquired waveforms used for analysis. (a) Signal received from direct transmission of one transmitter. This signal was used as the reference to compare the focusing results. (b) Waveform acquired when two transmitters were used to generate a focal zone. (c) Signal received from three-transmitter configuration.

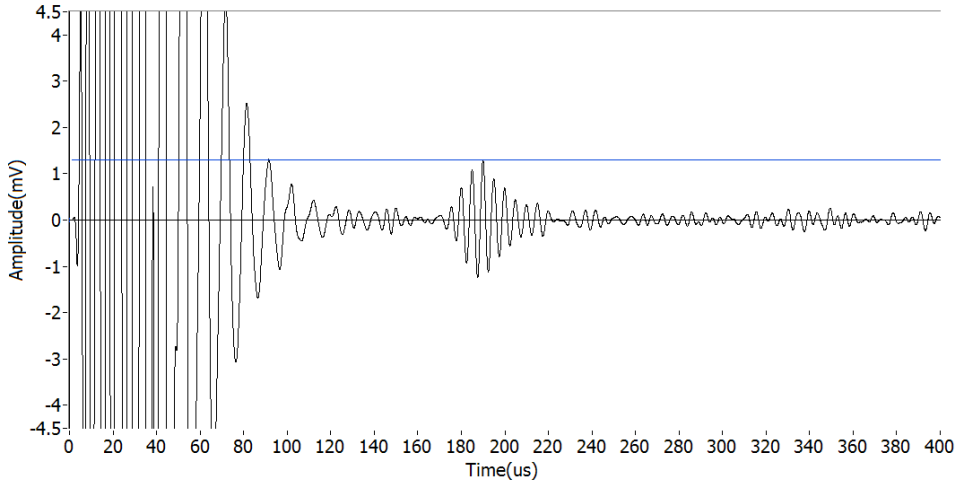

Figure 5.2. RF waveform acquired after moving the receiving EMAT 3 in. past the focal point of the 3-EMAT focused array. Signal amplitude decreased by 10.14 dB confirming that the array has a focal point at the designed distance of 19 *in*.

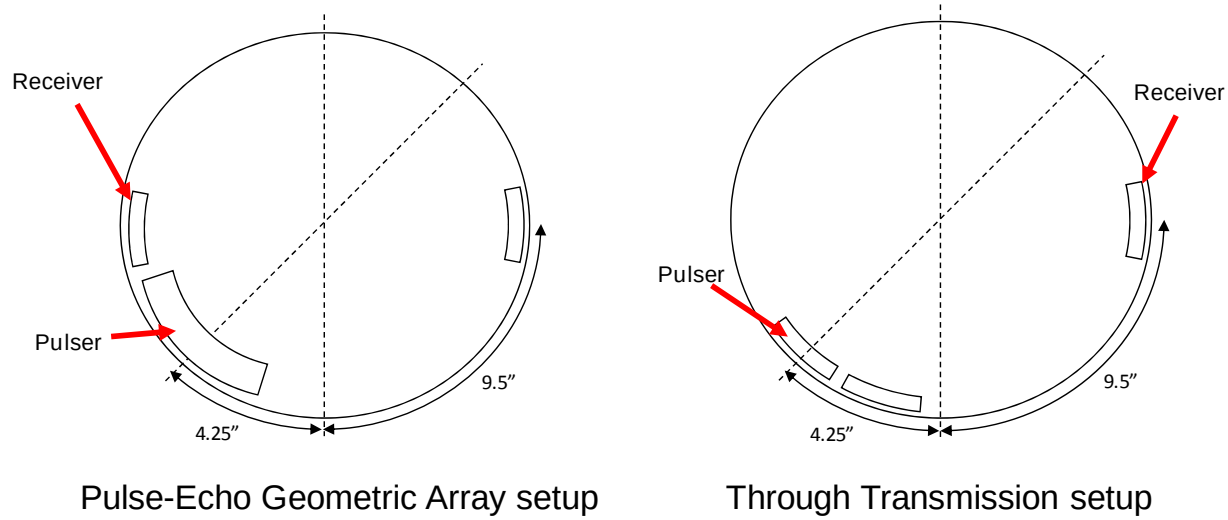

Figure 5.3. Primary sensor configurations used for data acquisition using the prototype ILI tool.

After experimentally verifying the benefits of a geometrically phased-array on a plate, a prototype ILI inspection tool capable of deploying the geometric phased array, as well as other sensor configurations, was designed and built. Figure 5.3 shows the two primary configurations used for data acquisition using the prototype ILI tools. For the pulse-echo configuration, details shown in Figure 5.4, a single large sensor housing has been designed to hold the geometric array. The bulk of the sensor housing is machined from aluminum and two Chromoly steel wear surfaces are fitted on either end of the sensor housing. The EMAT magnets are situated in a Noryl insert to avoid generating waves inside the aluminum housing itself. Special precautions

were taken, such as the use of bronze bushings, to maintain a common ground throughout the ILI tool, keeping electrical noise to a minimum. The tool configuration shown in Figure 5.4 was used primarily to examine reflections generated by defects in the focal zone of the EMAT array.

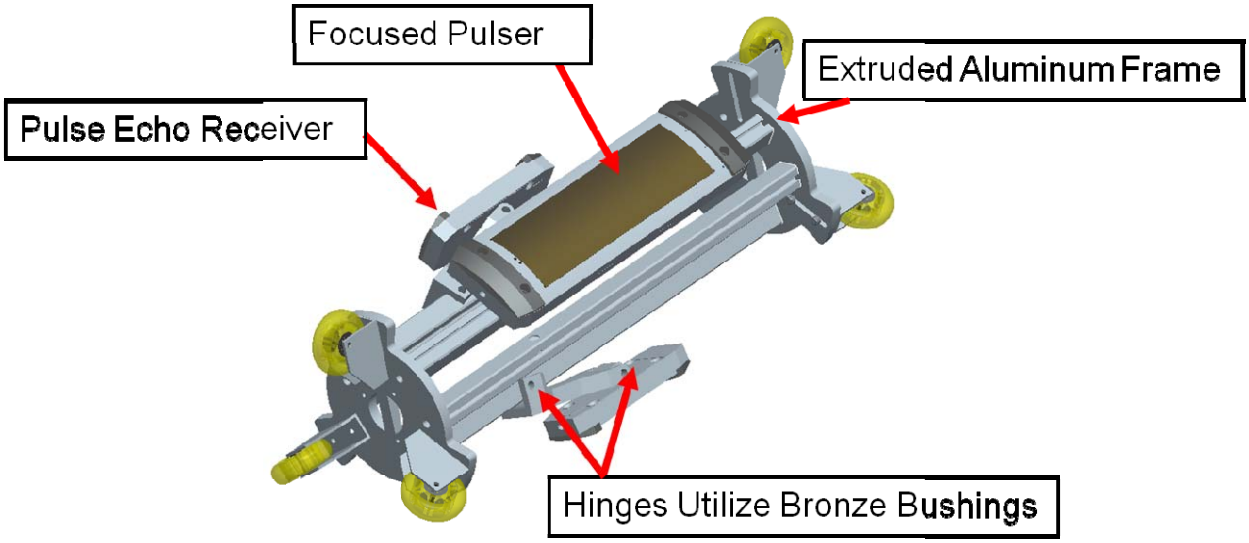

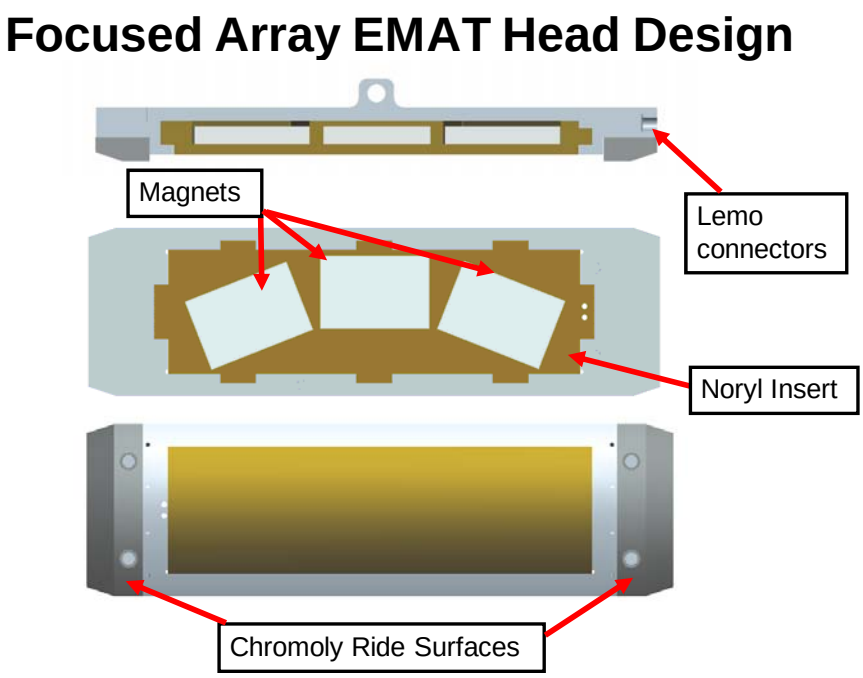

Figure 5.4. Details of the sensor configuration and design for pulse-echo measurements using the geometrically focused array.

Figure 5.5 shows the tool configuration used for through transmission measurements. In the through transmission configuration, a single curved coil was used to send waves through the defect region and to a received on the opposite side. All receivers used in this project were of the traditional straight coil design to ensure dominant reception in the propagation direction only. Three different coil designs used in the two different ILI tool configurations are shown in Figure 5.6. Also, photographs of the fully constructed ILI tools are shown in Figure 5.7.

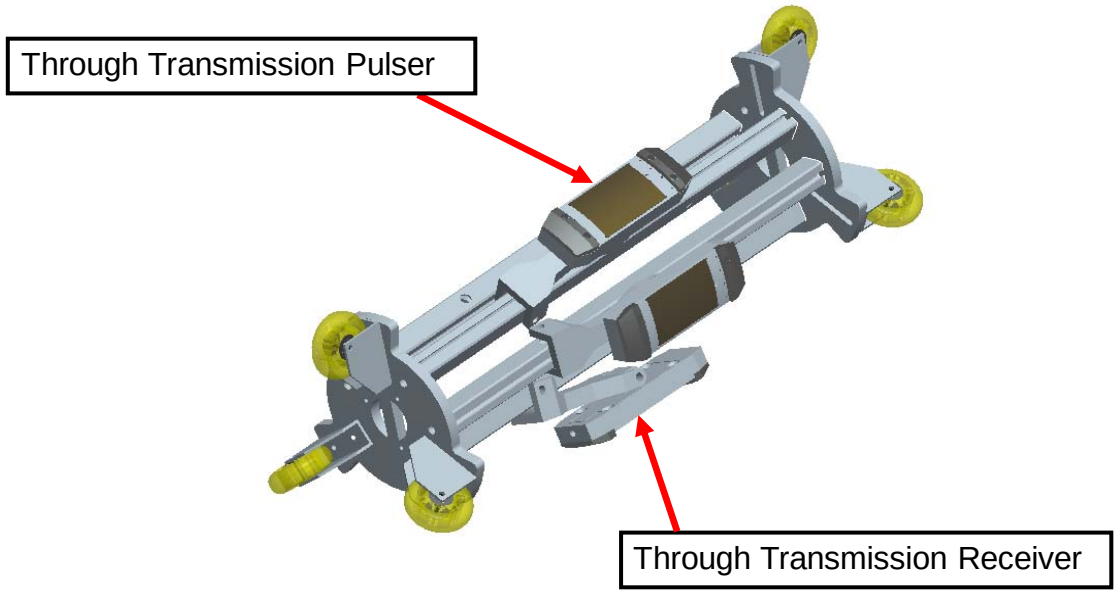

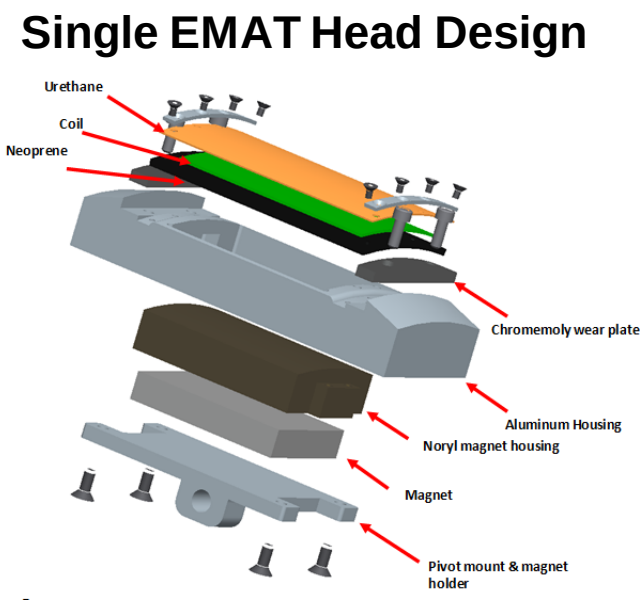

Figure 5.5. Details of sensor configuration and design used for through-transmission data acquisition.

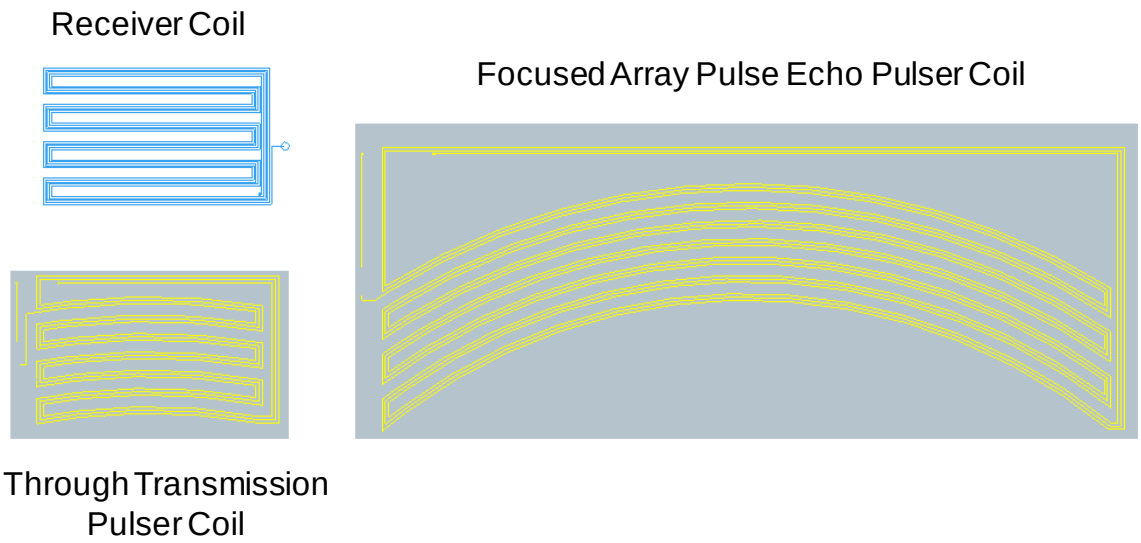

Figure 5.6. Three different EMAT coil designs employed in the two ILI tool configurations.

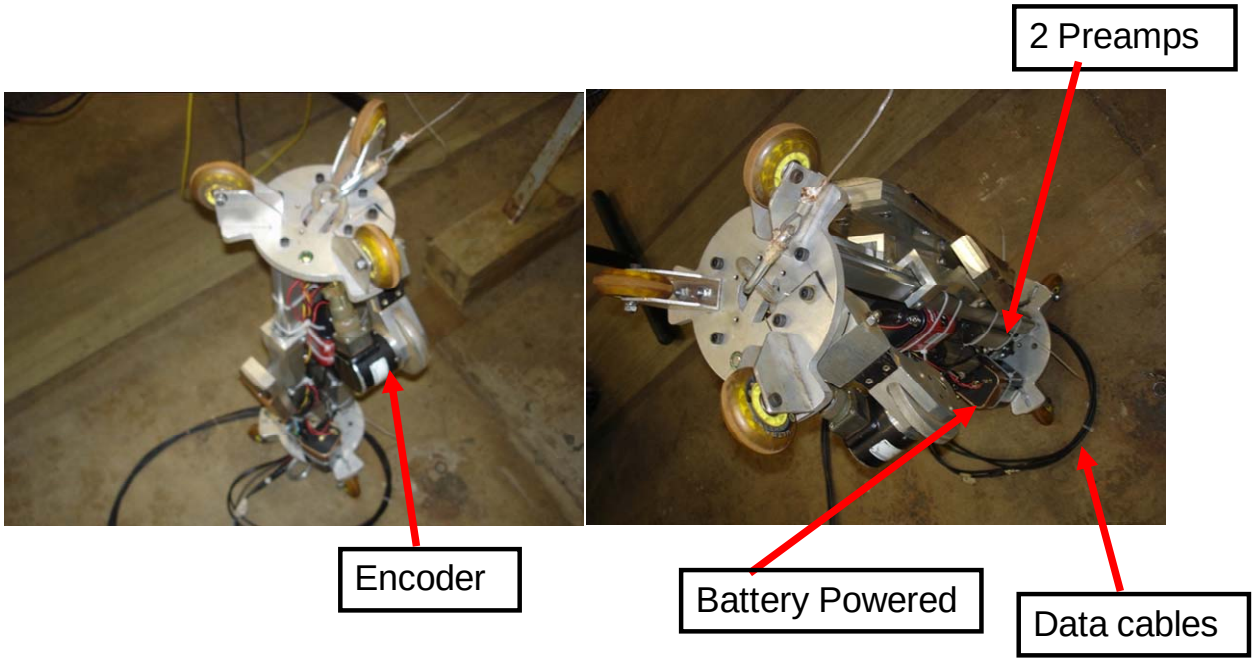

Figure 5.7. Photographs showing the completed prototype ILI tool for data acquisition.

Figure 5.8 shows a flow diagram between the key system components used for all experiments performed with the prototype ILI tool. The counts/in from the encoder are sent to the digital counter where they are up- or down-sampled to produce a trigger in the increments specified by the user in the software waveform setup controls. A trigger is then passed to the A/D card and the receiving channel is activated and the trigger is relayed to the arbitrary waveform generator (ARB). The ARB outputs +/- 1V rectangularly windowed sine wave of the desired frequency into the 1200V amplifier. The amplifier turns sine wave to 1200V square wave. The pulse then travels through the matching network, which matches the impedance of the transmitting coil. From the matching network, the pulse travels to the transmitting EMAT which generates a guided wave in the wall of the pipe. The guided wave travels through the pipe wall to the receiving EMAT. Because the received voltages are typically very low, the received pulse is sent through a pre-amplifier before it is passed to the A/D to be digitized, processed, and displayed on screen or sent to a storage device. The details of some of the key electronic components are summarized in Tables 5.2 through 5.4.

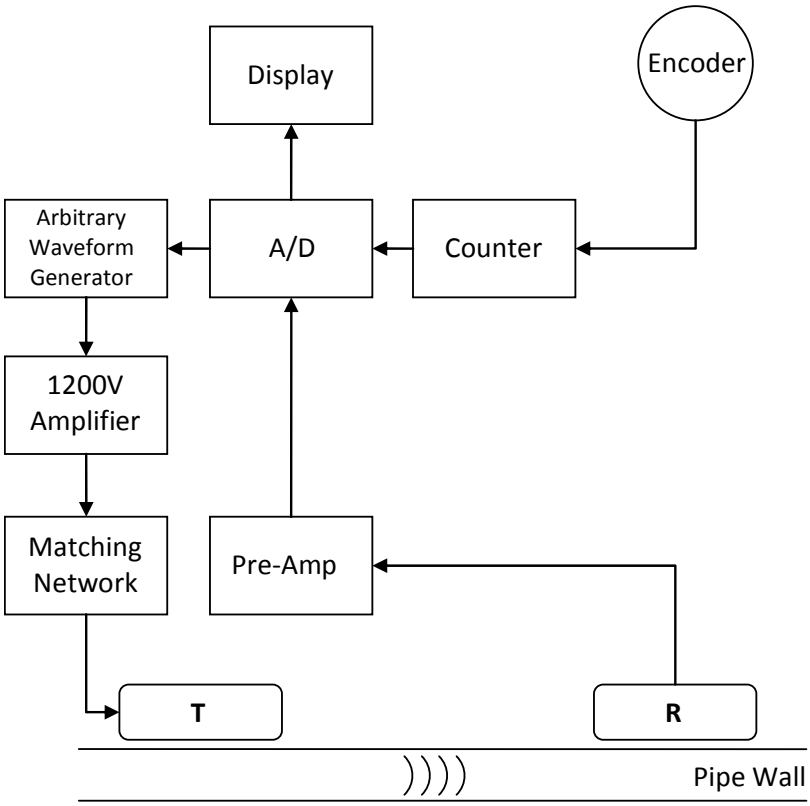

Figure 5.8. System flow chart showing key components.

Tables 5.2, 5.3, and 5.4 describe three of the primary electronic components that were used to complete the geometrical focusing experiments. They consist of an arbitrary waveform generator, A/D converter, and toneburst amplifier, respectively. These components were also used in all of the ILI experiments that will be presented shortly. Two other components that are

not shown below include a variable impedance matching network and pre-amplifier for the EMAT sensors.

Table 5.2. Arbitrary Waveform Generator

Analog output channels	1
Amplitude Range	10mV to 10V full scale (50 ohms)
Resolution	14 bit
Output Current	200mA peak
Sample clock	100 MSample/sec
Output bandwidth	100Hz to 15MHz
Memory	512 KSamples max
Operating Modes	Free run, programmable single shot, programmable repetitive, external trigger
Form factor	PCI full slot

Table 5.3. Analog-to-Digital Converter

Resolution	8 bit
Bandwidth	100 MHz max, 20 MHz typical
Sample clock	100 MHz
Channels	2 Simultaneously sampled
Memory	16 MB
Vertical range	+/- 25mV to +/- 25V
Trigger	External edge
Trigger range	+/- 10V

Table 5.4. Toneburst Amplifier

Mode	Square wave
Output	+/- 600 V

Figure 5.9 shows two screenshots from the waveform processing and display software developed by FBS, Inc. for displaying ILI data. The "Waveform" screen (top) contains all waveform-filtering options and the "Averaging" screen (bottom) contains options for spatial signal averaging. Spatial averaging is employed because the sensor is never in one location long enough to perform temporal averaging. In the spatial averaging algorithm, the waveform obtained at the indicated position is averaged with the waveforms to the right and left of the indicated position. The user can input the number of waveforms to be averaged. Typical averaging numbers include 3, 5, or7 waveforms.

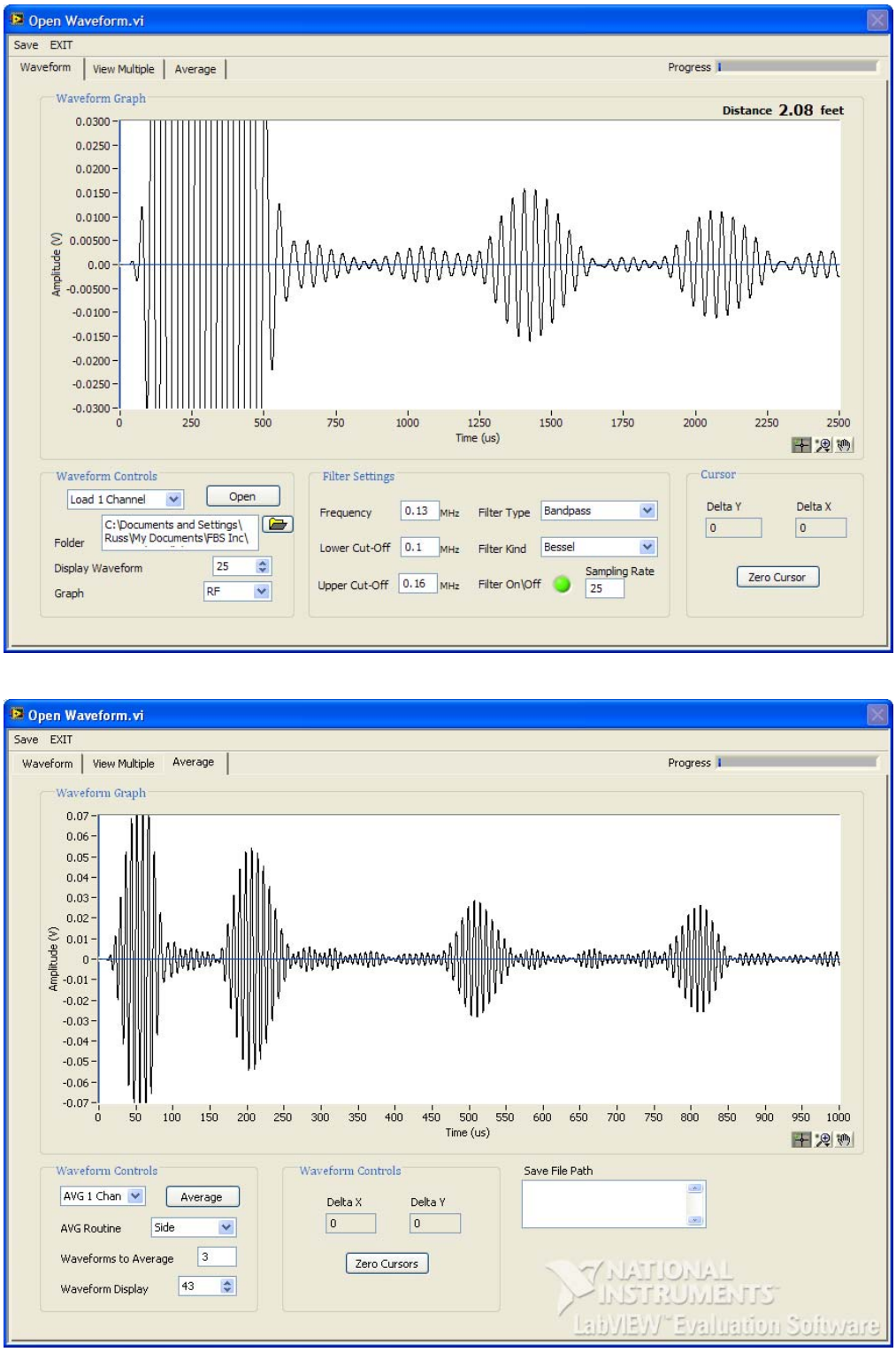

Figure 5.9. Screenshots of waveform display software developed for processing and viewing ILI data. Top screen contains filtering settings and bottom screen shows spatial averaging options.

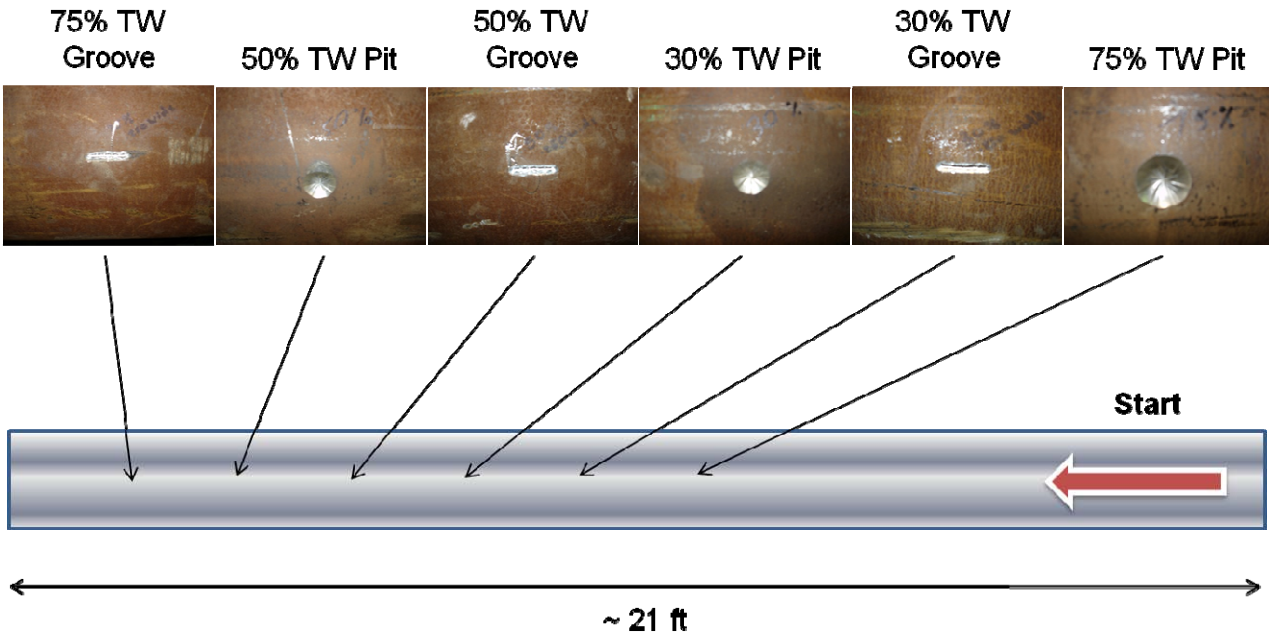

Figure 5.10. Schematic showing defect location and detail in the 12 *in* 0.375 *in* wall thickness X52 verification specimen.

Figure 5.10 shows a schematic of the 12 *in* 0.375 *in* wall X52 pipe specimen that was used for verification of the analytical and numerical modeling. As seen in the figure and described in Table 5.5, the pipe specimen had six defects: three axial grooves and three simulated pits. The axial grooves were all ~1.5 *in* long and 0.25 *in* wide with depths of 30%, 50%, and 75% through wall. The simulated pits were approximately 0.5-0.75 *in* in diameter depending on the through wall depths, which were also 30%, 50%, and 75%. The axial location along the pipe of each defect is listed in Table 5.5.

Table 5.5. Defect details in the 12 *in* schedule 40 X52 verification specimen.

Distance (in)	Defect type	Depth
75	circular	75%
100	elongated	30%
125	circular	30%
150	elongated	50%
175	circular	50%
200	elongated	75%

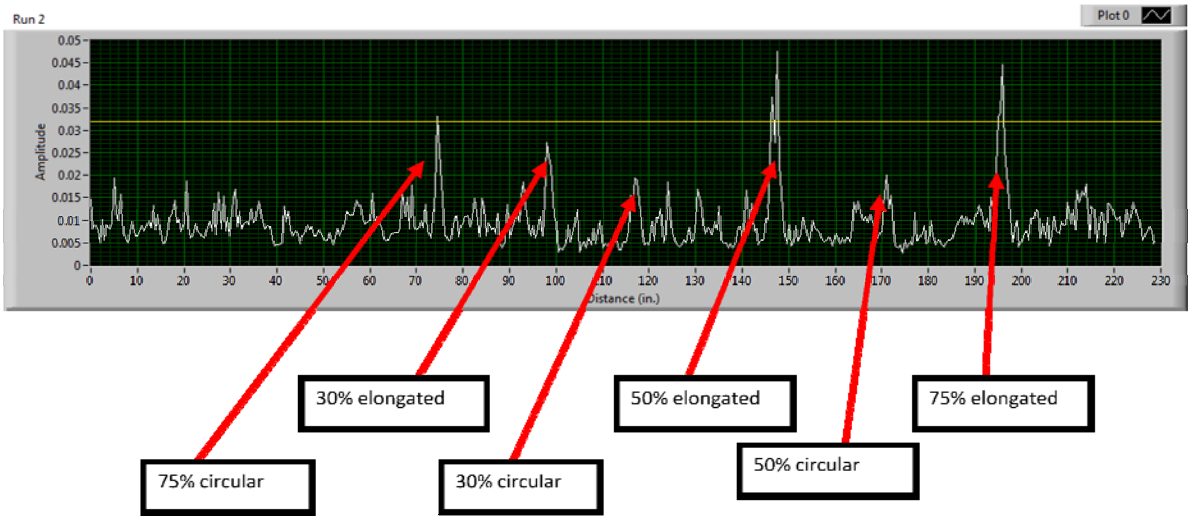

Figure 5.11. Unfiltered and unaveraged defect amplitude data for 12-*in* verification pipe. Note that all defects are identified without the use of any signal processing.

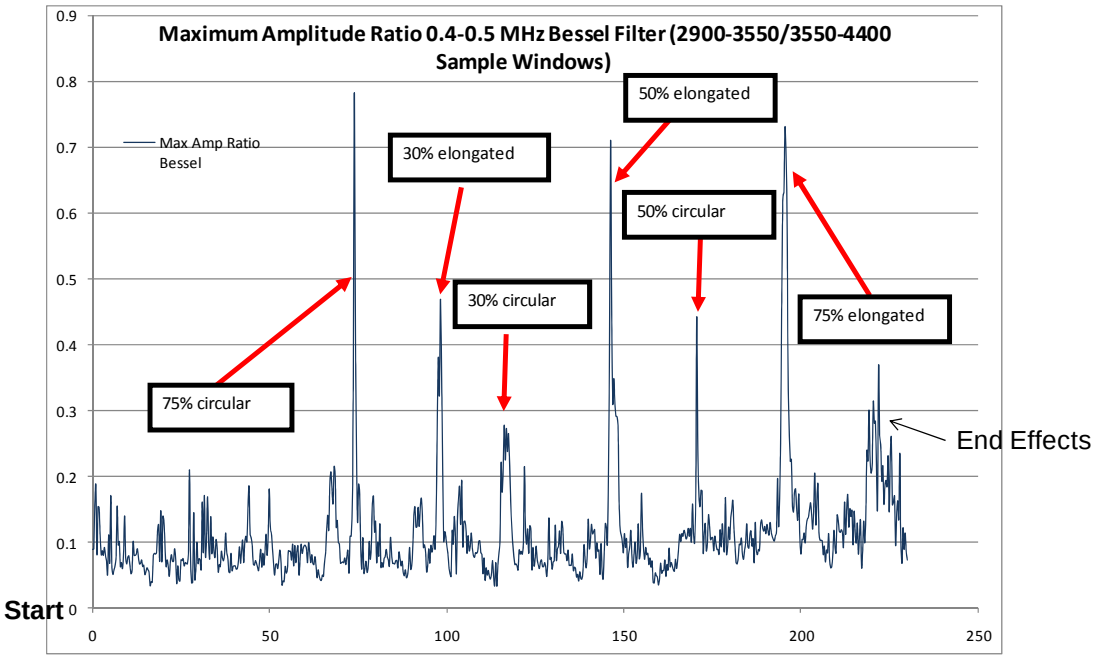

Figure 5.12. Filtered and normalized amplitude data for 12-*in* verification pipe. Note that normalized amplitude information accurately ranks each defect according to depth for each defect class. The different classes can be differentiated by comparing the A0 and S1 data.

Figure 5.11 shows the result obtained using the pulse-echo geometric array configuration and the 456 *kHz* S1 mode. It should be noted that the result shown in Figure 5.11 has not been filtered or averaged and therefore the noise floor is slightly high. Figure 5.12 shows the same data set after being filtered and normalized using the latent backward propagating wave amplitude. It is seen that the normalized amplitude correctly predicts the relative defect depths for the two classes of defects. Though not shown here, it was found the 200 *kHz* A0 mode was relatively insensitive to the simulated pit defects, though it was able to accurately rank the groove type defects according to size. It is therefore possible to separate the two classes of defect by using a multi-mode inspection.

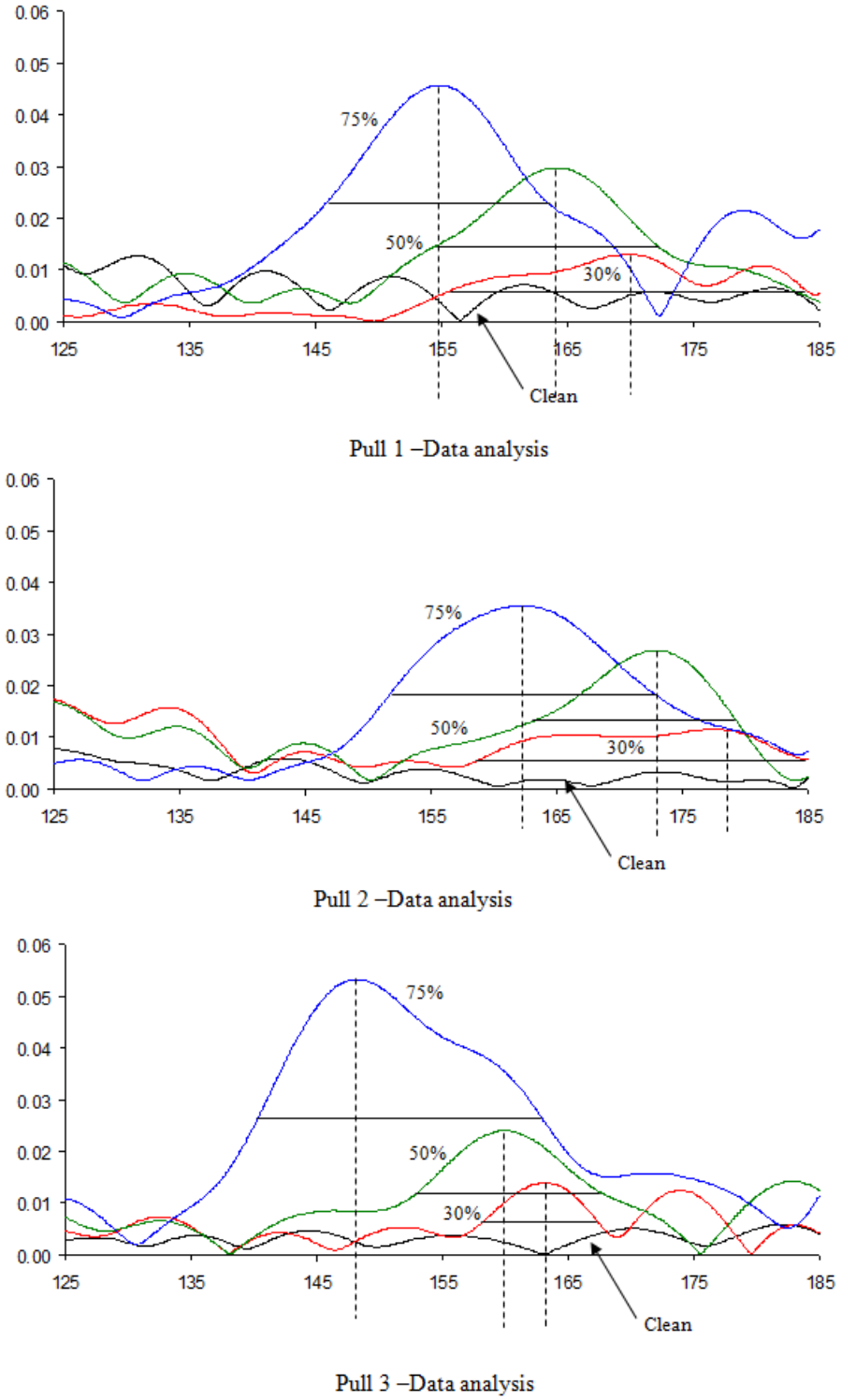

Figure 5.13. Three different data sets obtained from the simulated pit defects showing both amplitude and time-based detection and sizing features.

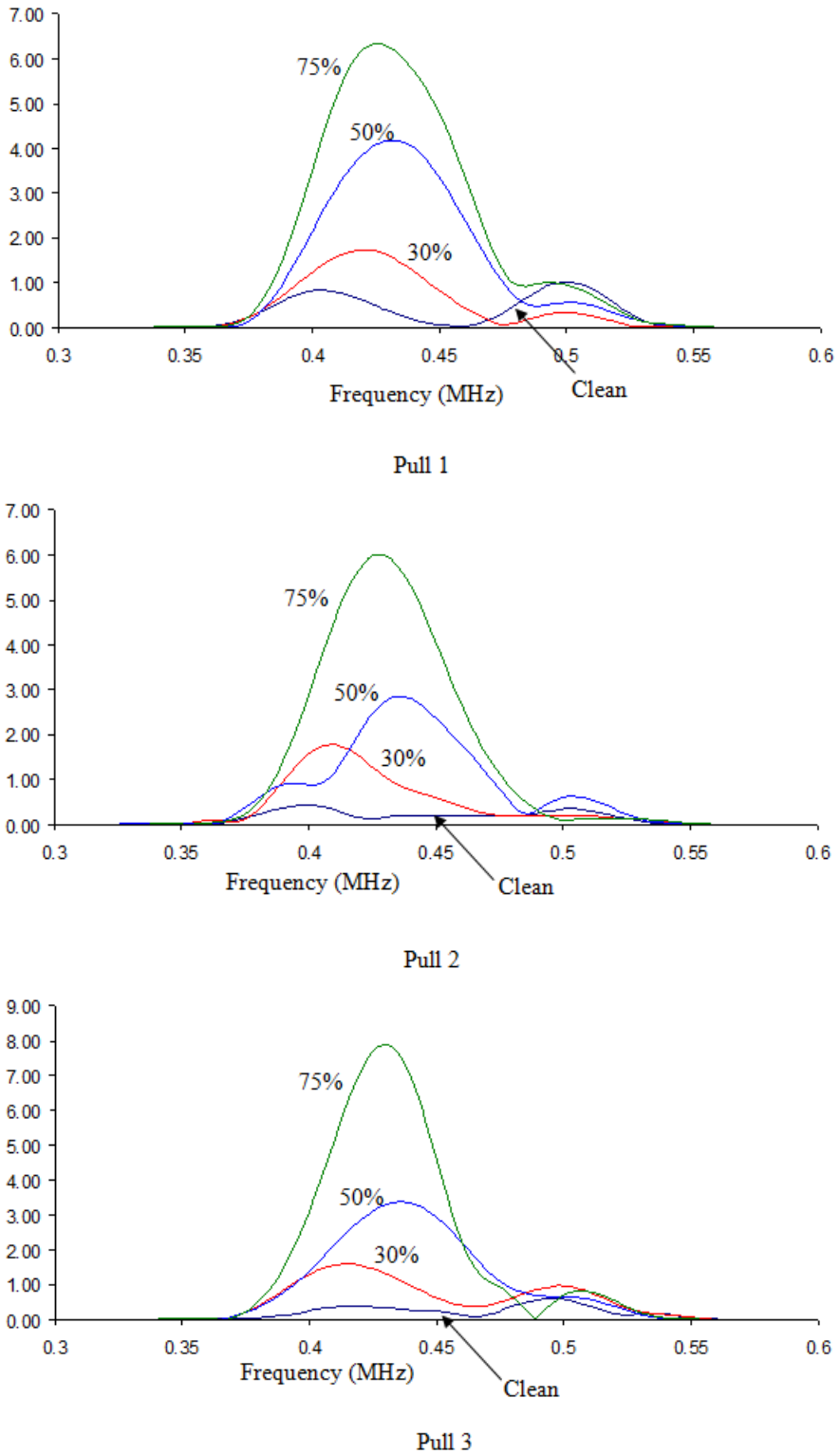

Figure 5.14. Three different data sets obtained from the simulated pit defects showing both frequency-based detection and sizing features.

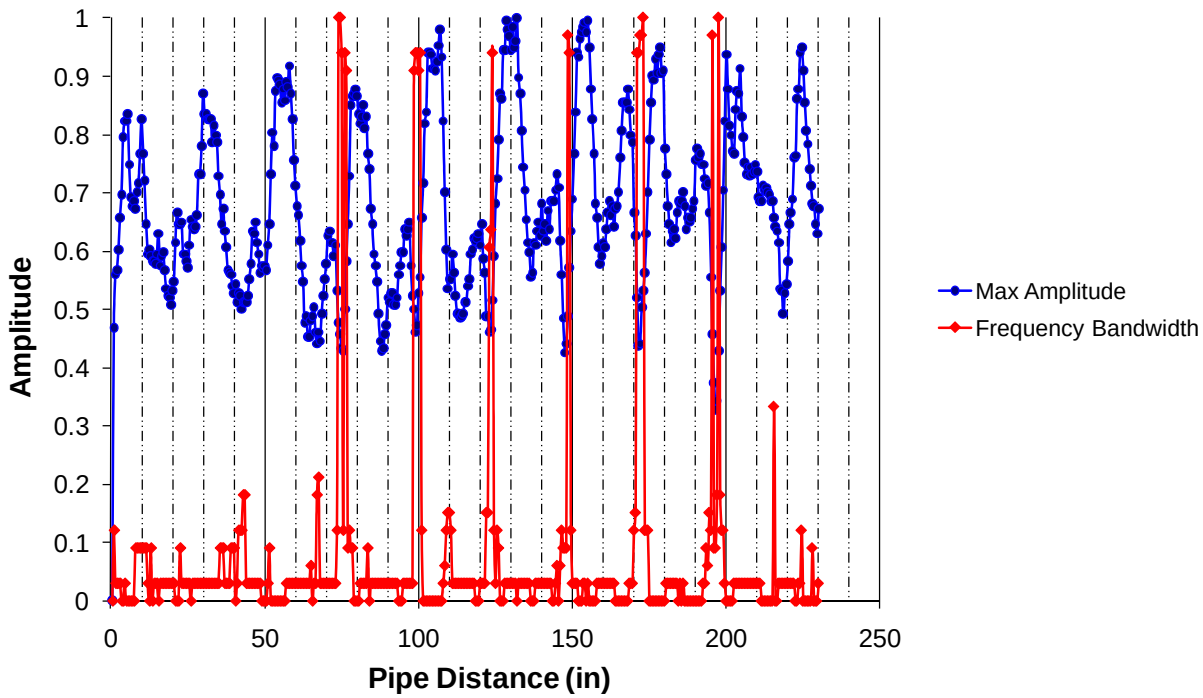

Figure 5.15. Through transmission data taken on 12 in schedule 40 X52 pipe. Data shows that frequency bandwidth is an excellent detection feature. Max amplitude data shown is unfiltered and unaveraged.

Figure 5.13 and 5.14 show the analytic envelopes of the wave energy reflected from the simulated pit-defects and the frequency content of the energy, respectively. In addition to the obvious amplitude feature seen in Figure 5.15, it is seen that as the depth of the defect increases, the relative time-of-flight decreases. This is effectively a manifestation of the increasingly inclined reflecting face of the deeper pits and can therefore be used as an additional sizing feature. This is a significant finding as time-based features are generally more reliable than amplitude features since they are not as easily corrupted by noise and sensor variations.

Figure 5.14 shows the same data sets as Figure 5.13 but in a frequency domain representation. It is seen that the amplitude of the FFT is another excellent predictor of pit depth. Furthermore, it appears as though the shallowest pit state (30%) tends to reflect low frequency energy than the deeper states. There appears to be some non-linear trend in the center frequency of reflected energy though more work is needed to verify this. Though maybe not an independent sizing feature, the center frequency could be included in a pattern recognition approach to the sizing of pits.

Figure 5.13 shows the amplitude (blue line) and frequency bandwidth (red line) information extracted from the data obtained using the through transmission configuration on the verification pipe. It is seen that the frequency bandwidth feature, while not necessarily well correlated with size, provides an excellent detection feature. To obtain this plot, an FFT of the wave transmitted through the defect region is calculated and the 6 *dB* down bandwidth is plotted. Again, this is another feature that, by itself, will not provide much information about sizing but will add

robustness and increase certainty for a pattern recognition detection and sizing algorithm. Note that the maximum amplitude data plotted in Figure 5.15 is unfiltered and unaveraged and is therefore noisy.

After verifying the new sizing techniques using the control pipe, it was important to demonstrate the applicability of the methods on pipes with naturally occurring corrosion that were pulled from service. Figure 5.16 shows two photographs of the inside of a 12 *in* 0.375 wall thickness steel pipe supplied by ConocoPhillips. It is seen that there is severe pitting corrosion along a relatively straight line that was most likely the bottom of the pipe when it was in service. The pipe samples with internal corrosion were characterized as part of another project and provided for use on this project. The pipe was transported to Battelle, cleaned, painted, and documented on another project for testing classical MFL tools. More than 100 internal corrosion anomalies were characterized using automated ultrasonic testing (AUT). Figure 5.17 shows typical AUT results. Also, the ID of the pipe was photographed to provide additional detail of the shape of the corrosion anomalies. It should be noted that photographing the inside of a pipe is difficult because of lighting challenges. The images of two corrosion anomalies are shown in Figure 5.18. To some readers, these pits appear as deposits, the inverse of the actual result, a common optical illusion.

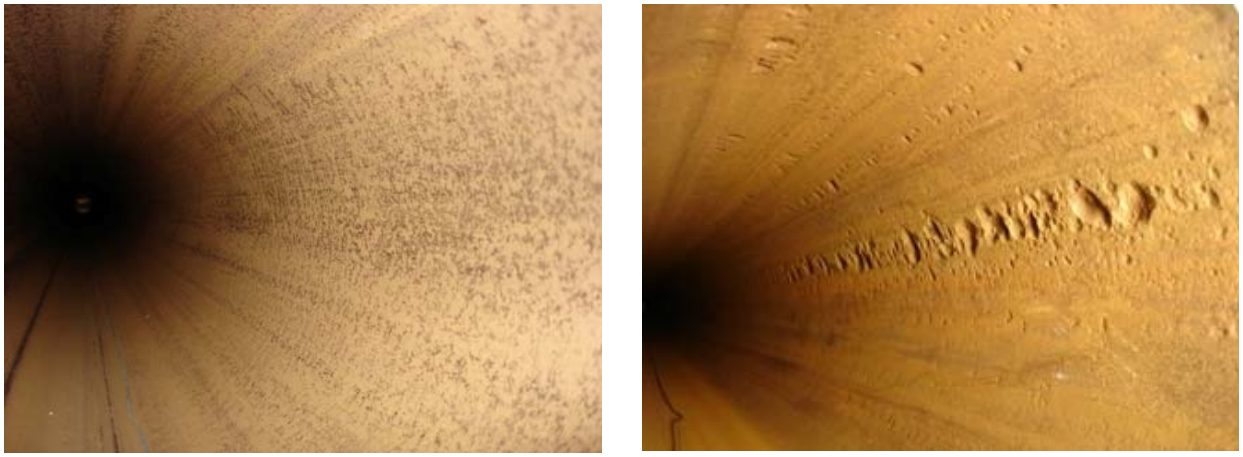

Figure 5.16. Photographs of clean (left) and pitted (right) section of the 12 *in* schedule 40 pipe sample that was removed from service.

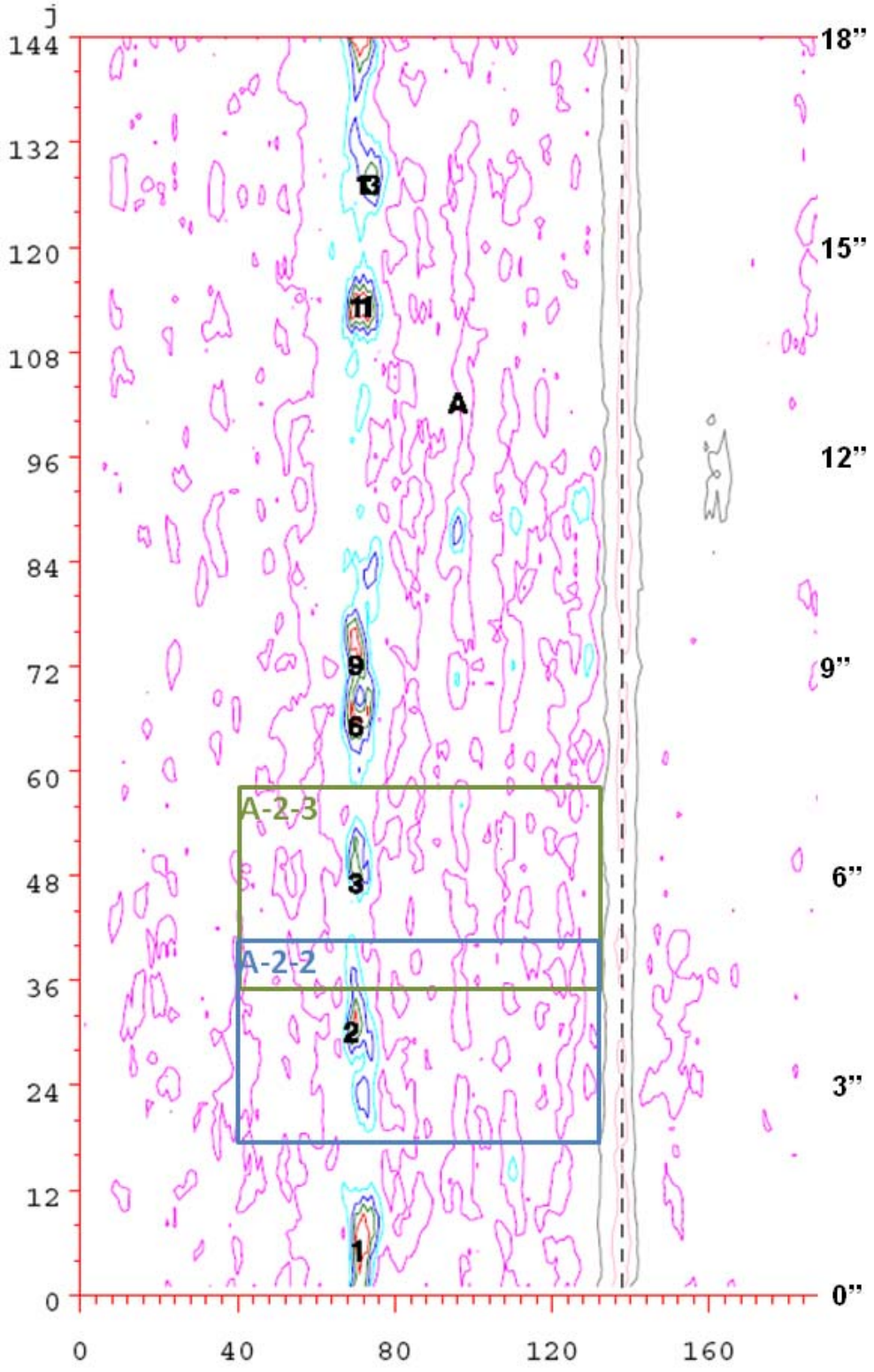

Figure 5.17. Automated ultrasonic scan of the pipe sample.

A-2-3 44.3%D 1.1"L 0.8"W

A-2-2 39.5%D 1.6"L 1.0"D

Figure 5.18. Photograph of ID corrosion corresponding to the boxes in Figure 5.13.

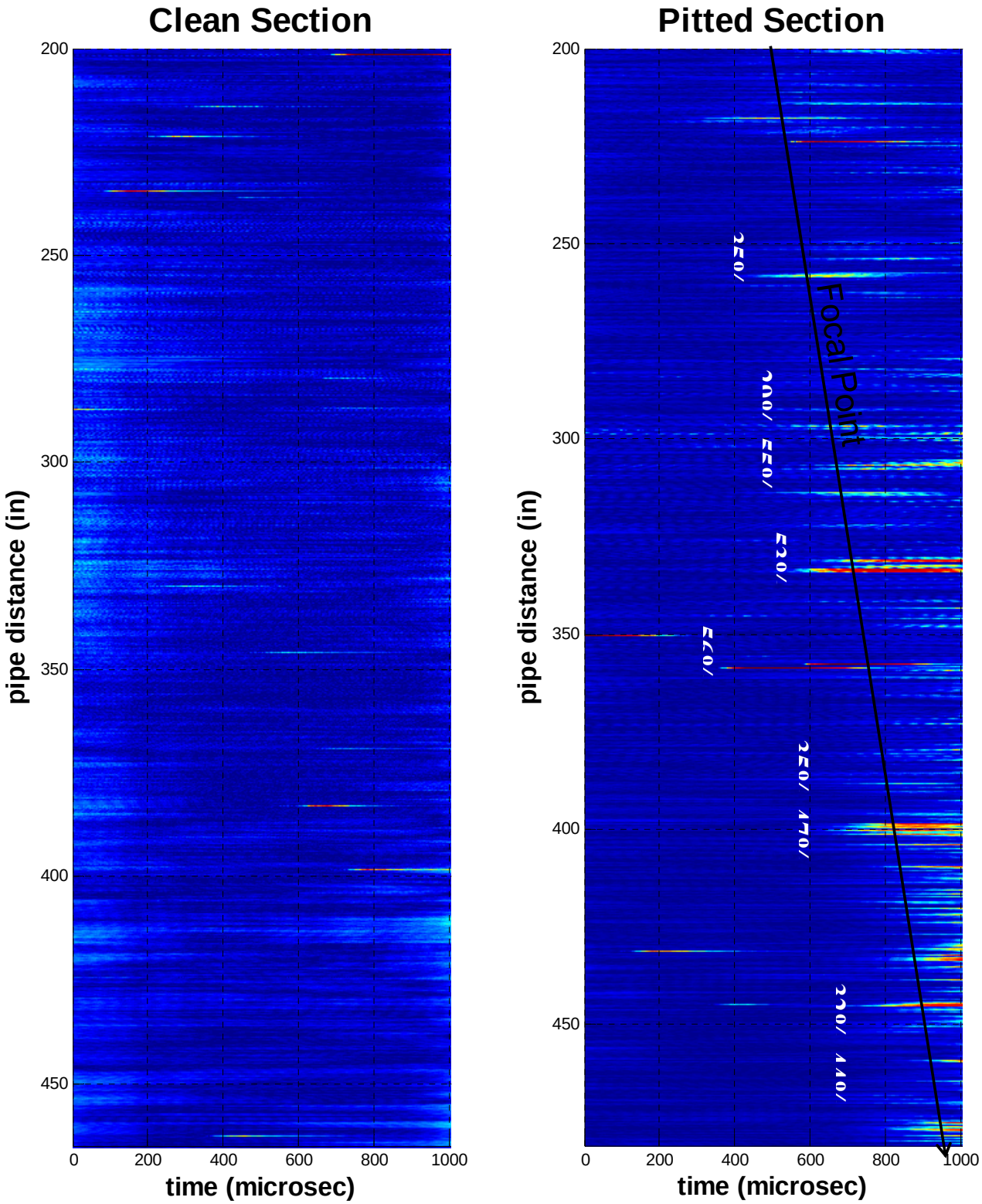

Figure 5.19. Pulse-echo pull data obtained on r natural corrosion pipe section. Note that the tool rotated as it was pulled through the pipe and caused the focal point to rotate out of the defect region.

Both pulse-echo focusing and through-transmission data were acquired on this pipe sample using the prototype ILI tool. For both sensor arrangements, data was collected in the clean section of the pipe and in the pitted section of the pipe using the 456 *kHz* S1 mode. Figures 5.19 through 5.27 present the results from these tests.

Figure 5.19 shows two 3D plots that were calculated using the pulse-echo focusing data sets acquired from the natural corrosion pipe specimen. The plot on the left corresponds to the case in which a clean (i.e. no pitting) section of pipe was located at the focal point of the geometric array. The plot on the right corresponds to the case in which the line of pitting defects was located at the focal point of the geometric array. By comparing these two plots, it is seen the focused array performed very well in detecting the corrosion pits. Furthermore, as indicated by the through-wall percentages on the plot, the focusing technique did a very good job at predicting the relative severity of the pits. It should be noted that because the tool rotated while being pulled through the pipe, the focal point was no longer aligned with the row of pitting defects by the time the tool reach the end of the pipe. This is obvious as the relative time-of-flight of the pitting indications increases as the tool moved down the pipe. This rotating may also have slightly affected the actual amount of energy being reflected from the pits, as the focal point was no longer perfectly aligned. In the future, real-time phased arrays can easily compensate for such rotation.

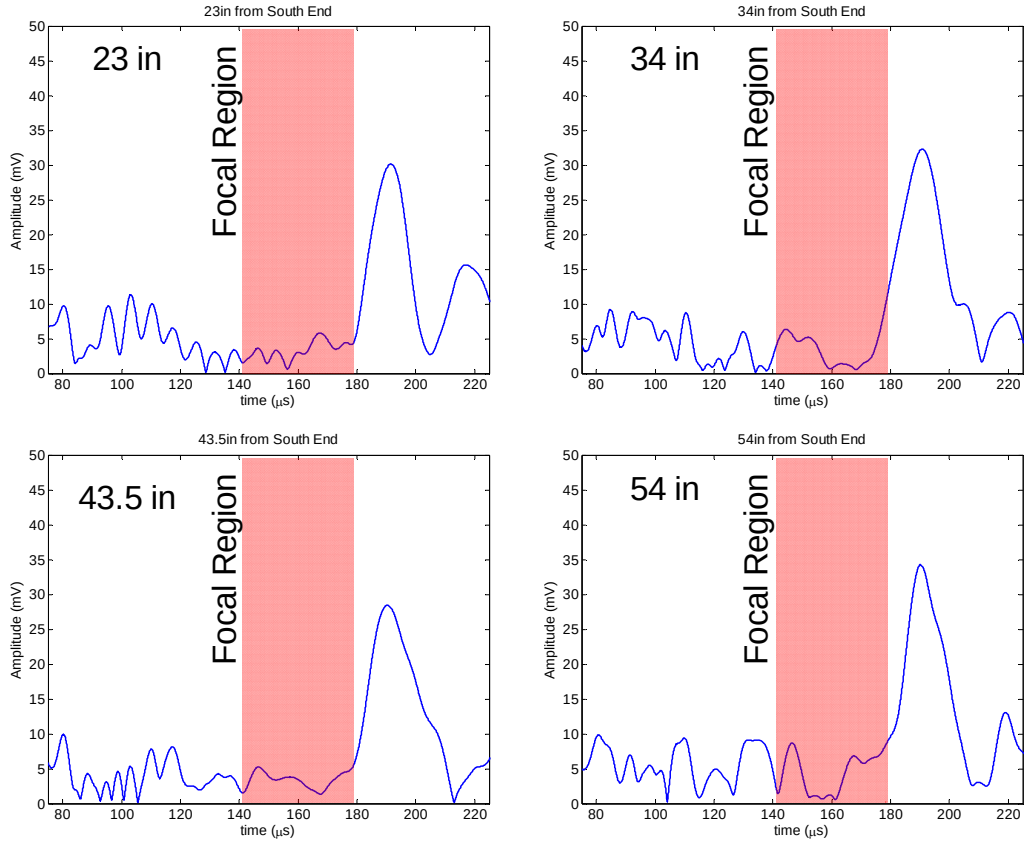

Figure 5.20. Analytic wave envelopes from several random locations within the clean section of pipe. Note that there are no reflections in the focal region that are above the noise floor.

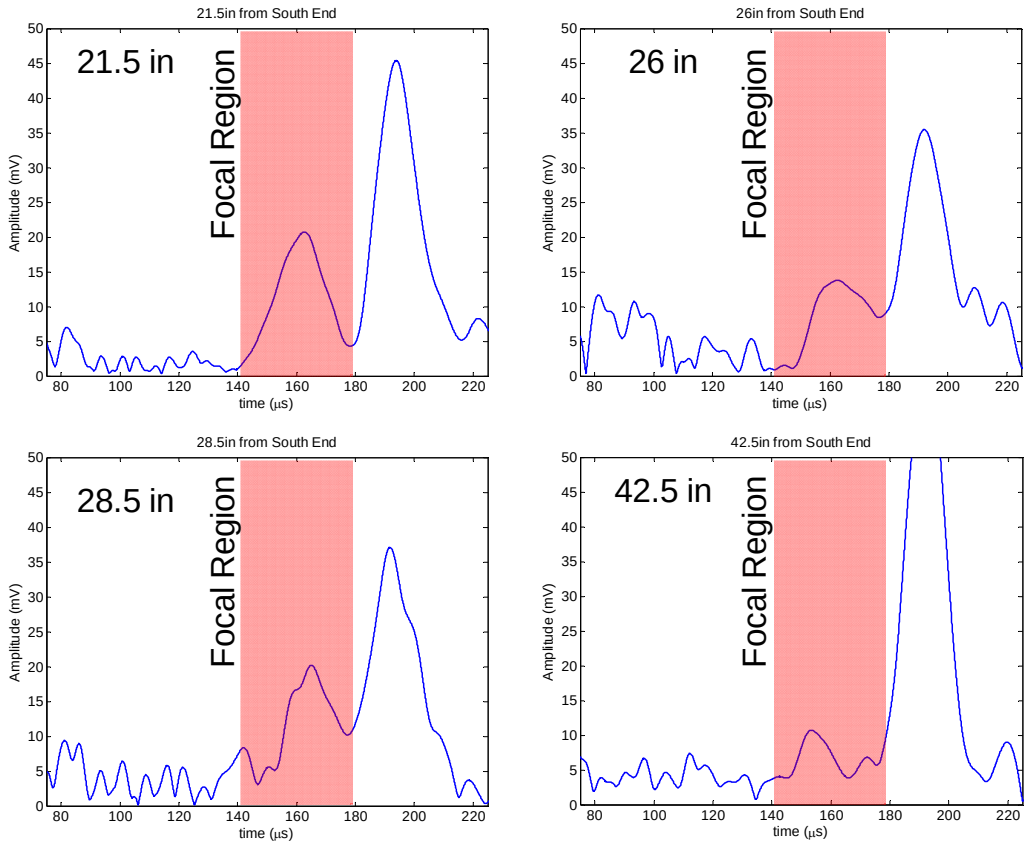

Figure 5.21. Analytic wave envelopes from several random locations within the pitted section of pipe. Note that there are obvious reflections in the focal region that are well above the noise floor.

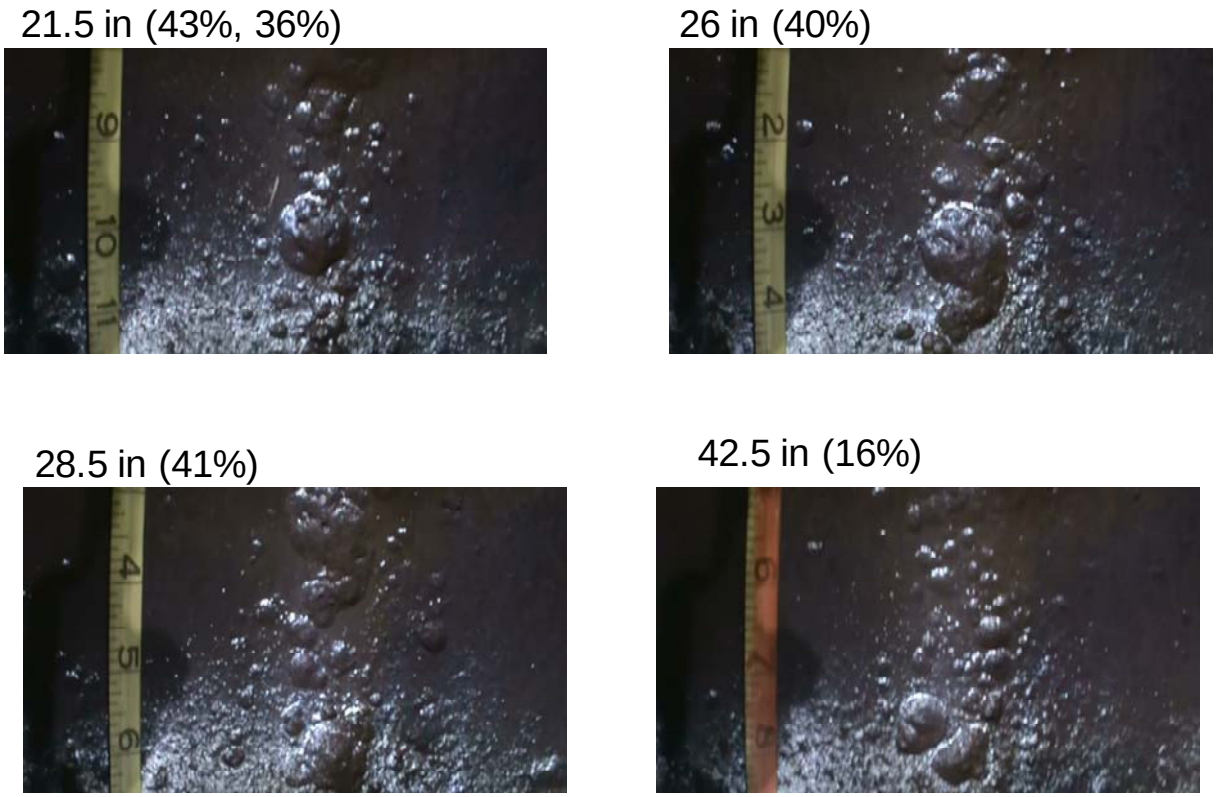

Figure 5.22. Photographs of the inside pipe surface at the locations corresponding to the data sets in Figure 5.20. Note that the percentages are the depth of the pits relative to the original thickness of the pipe.

Figure 5.20 shows several analytic wave envelopes, taken at random, from the clean section of pipe. The focal point of the geometrically focused array is highlighted in red and it is seen that there are no discernable reflections rising above the noise floor in any of these plots. The distances indicated on each of the plots were measured from what was the south end of the pipe at the time of acquisition. Figure 5.21 shows similar plot but for data that was acquired with the row of pitting corrosion located at the focal point of the array. It is clear that substantial reflections are received from the pitting defects. Photographs of the pitting occurring at distances shown in Figure 5.21 are shown in Figure 5.22 along with the percent through wall depth of the defect(s) in that area. Note that all the reflected wave packets are similar in amplitude except for the one in the lower right plot. This is expected as the reflections that are similar in amplitude are all from pits that are near ~40% through wall while the one reflection that is lower in amplitude corresponds to only a 16% through wall pit. This is further verification of the sizing capabilities of the newly developed ILI focusing technique.

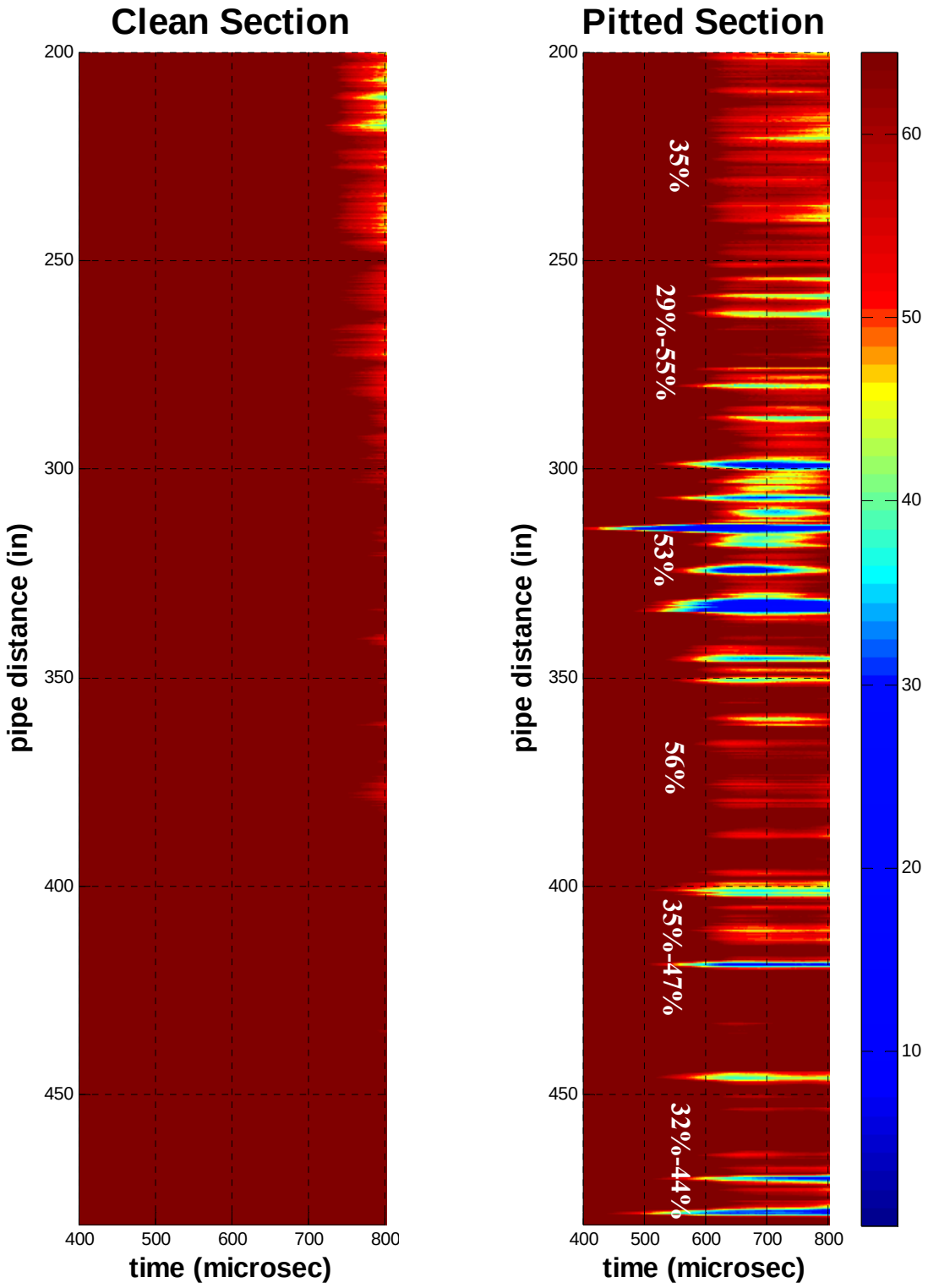

Figure 5.23. Through transmission pull data obtained on retired pipe section at Battelle PSF facility.

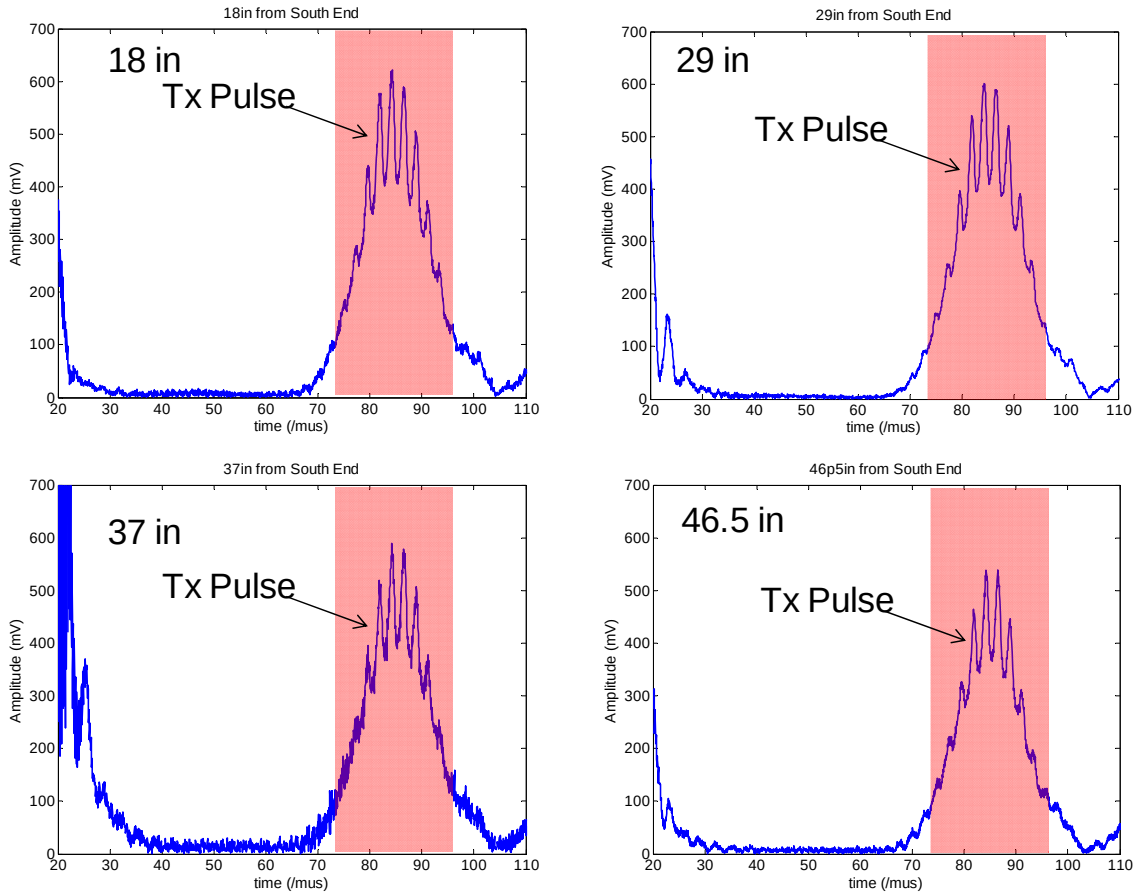

Figure 5.24. Through transmission analytic wave envelopes from several random locations within the clean section of pipe. Note that the amplitude of the through transmission pulse is high and very comparable at the different locations.

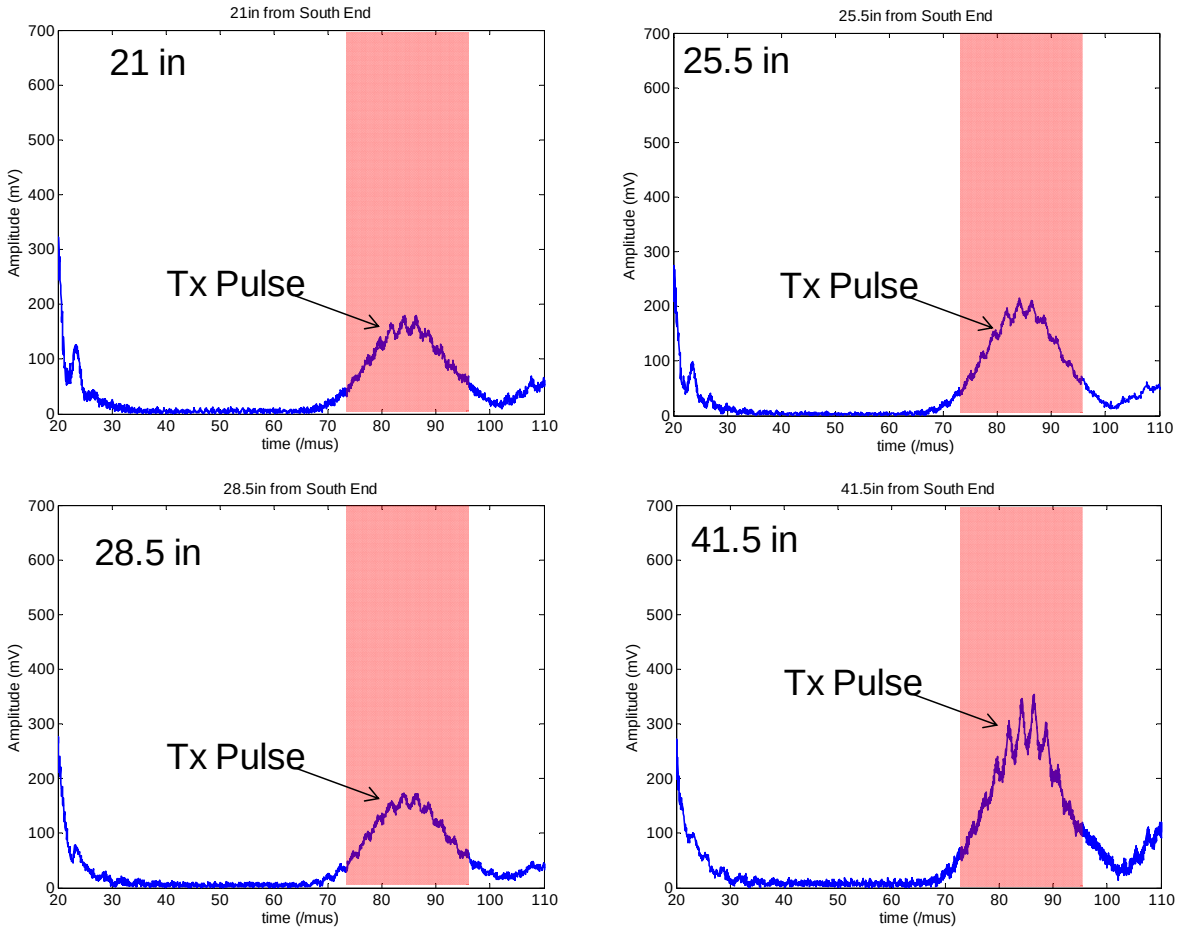

Figure 5.25. Through transmission analytic wave envelopes from several random locations within the pitted section of pipe. Note that the amplitude of the through transmission pulse is low and correlates well to the depth of the pits as indicated in Figure 5.21.

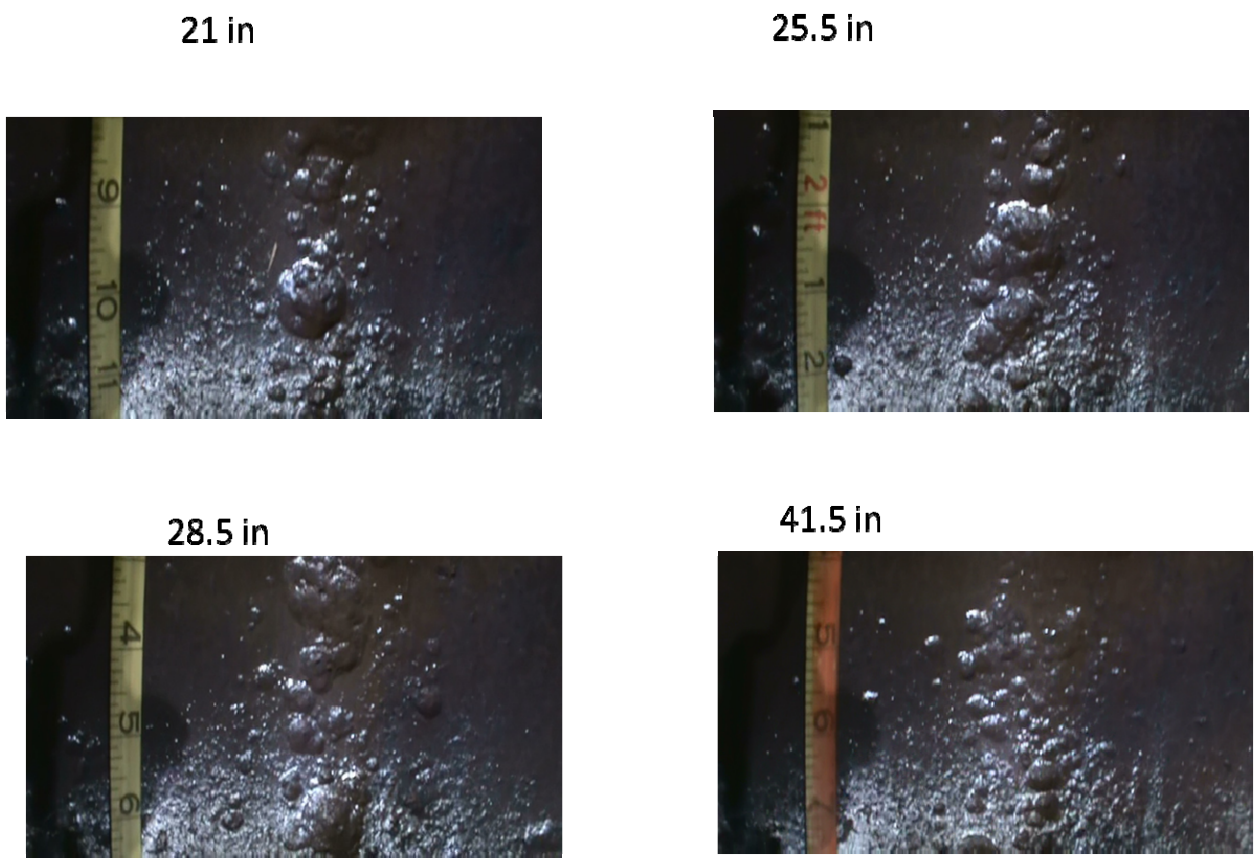

Figure 5.26. Photographs of the inside pipe surface at the locations corresponding to the data sets in Figure 5.24. Note that the depths of these pits are indicated in Figure 5.21.

Figure 5.23 shows a similar set of plots as Figure 5.19 but for the through transmission data. Again, the 3D plot on the left corresponds to the clean section of pipe while the 3D plot on the right corresponds to the section of pipe that contains significant pitting. It is again seen that the through transmission data is highly sensitive to the pitting defects. The relative intensity of the indications seen in the plot on the right correlate well with pit depth, though the plot has been slightly saturated for easy viewing.

Figure 5.24 shows several randomly selected analytic wave envelopes of the through transmission data obtained in the clean section of pipe. It is seen that the fluctuation in amplitude between these four signals is negligible while the through transmission analytic wave envelopes obtained in pitted section, shown in Figure 5.25, show significant reductions in transmitted wave amplitude. Note the defect locations shown in Figure 5.25 were chosen to be as near as possible to those positions shown in the pulse-echo data of Figure 5.21. Again, it is seen that the reduction in amplitude of the wave transmitted through the defect region is uniformly high for the three pits that are ~40% deep and less so for the 16% through wall pit. Figure 5.26 shows the available photographs of the pitting regions corresponding to the data displayed in Figure 5.25.

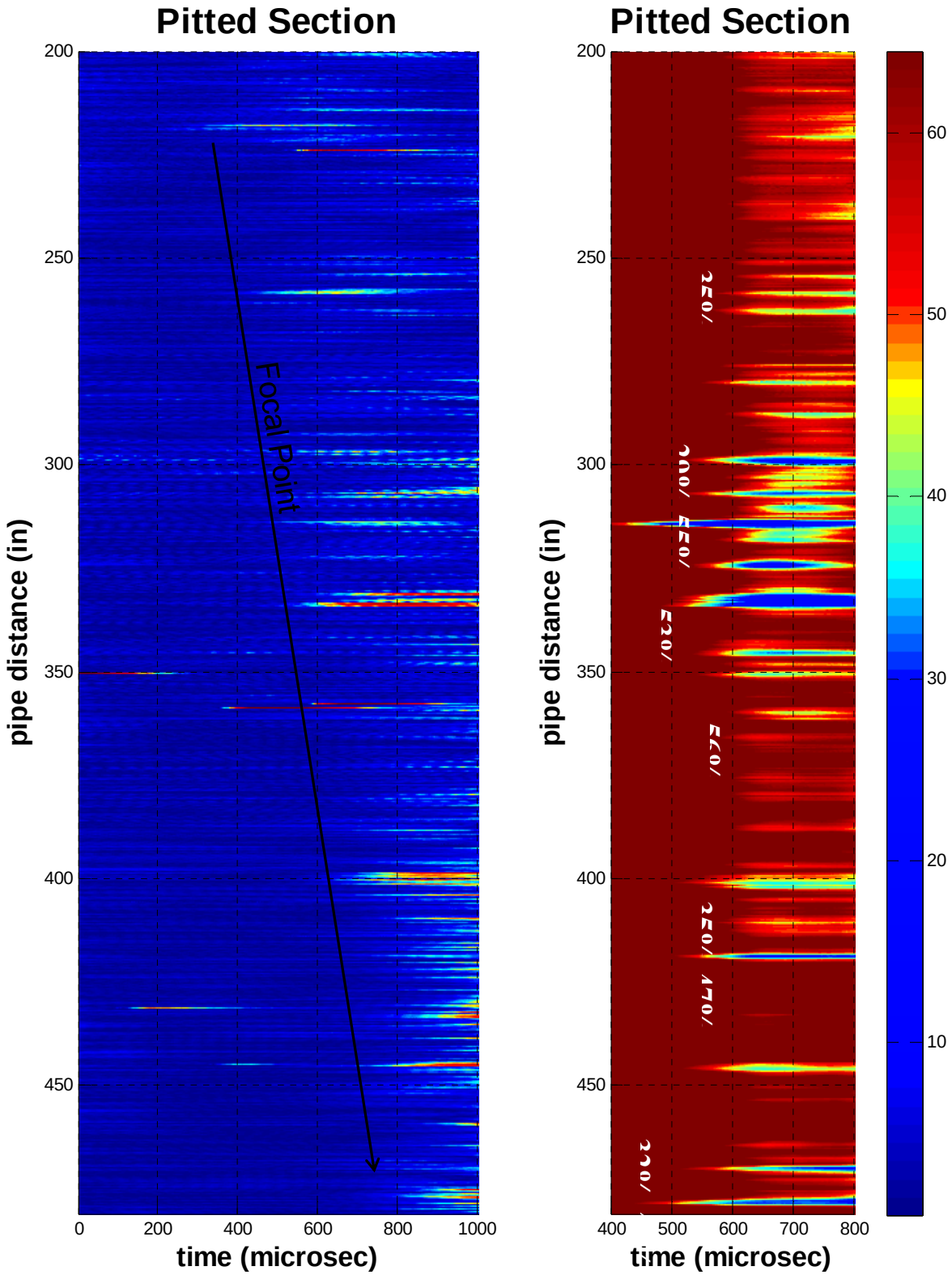

Figure 5.27. Side by side comparison of focused pulse-echo (left) and through transmission (right) data sets. Note excellent correlation between defect locations and relative severity.

Finally, Figure 5.27 shows a side-by-side comparison of the pulse-echo focusing and through transmission data obtained in the pitted section of pipe. Excellent correlation is seen between the two plots for both the defect location and relative intensity. This successfully demonstrates the viability of the detection and sizing technique for real pitting corrosion. The next and final section of this report summarizes the main points of this work and discusses the logical next steps toward integration with MFL technology and implementation in commercial tools.

6. CONCLUSION AND FUTURE DIRECTION

The motivation and primary goal of this development was to improve corrosion anomaly depth sizing of magnetic flux leakage (MFL) tools by adding phased array GWUT inspection technology. Some of the key contributions of this work are outlined below:

- Newly developed ILI focused array shows significant benefits over traditional EMAT coils (sensitivity, resolution, etc.).
- Demonstrated excellent potential for real-time phased array implementation.
- The pulse-echo EMAT array and through transmission configurations demonstrated defect detection and sizing capabilities.
- Relative amplitude, time, and frequency based sizing features were identified.
- The technique was successfully demonstrated on a section of pipe removed from service with severe pitting corrosion.

While the work presented here has successfully demonstrated the capabilities of guided waves for improving corrosion sizing estimates, there is still some work that should be done prior to or concurrently with the development of a commercially viable tool. Some topics to be addressed include:

- Migration to real-time phased array to replace geometrically focused array.
- Development of pattern recognition capability to meld MFL and GWUT data to provide optimized sizing information.
- Further validation and testing of different defect geometries.
- High(er) speed pull tests.
- Find implementation partner.

Because the guided-wave ILI market is still in its early developmental stages, and there are not many competing technologies available, there is significant opportunity to make lasting contributions in this area. It is strongly believed that some of the results of this work will eventually be incorporated into an industrial inspection technology. The details of this work were recently presented at the 16th US National Congress of Theoretical and Applied Mechanics. The conference information is as follows:

> Van Velsor, JK, Rose JL, Nestleroth, JB, and Zhang, L., "Improving Magnetic Flux Leakage In-Line Inspection Corrosion Sizing Using Phased Array Guided Ultrasonic Waves," *Presented at the* 16th United States National Congress of Theoretical and Applied Mechanics, State College, PA, 2010.

7. REFERENCES

1. Ghosh, J., *Longitudinal Vibrations of a Hollow Cylinder,* Bulletin of the Calcutta Mathematical Society, 1923/24, **14**: p. 31-40.

2. Mirsky, L. and Herrmann, G., *Nonaxially-Symmetric Motions of Cylindrical Shells,* The Journal of the Acoustical Society of America, 1957, **29**(6): p. 772-773.

3. Mirsky, L. and Herrmann, G., *Axially Symmetric Motions of Thick Cylindrical Shells,* Journal of Applied Mechanics, 1958, **80**: p. 97-102.

4. Gazis, D. C., *Three-Dimensional Investigation of the Propagation of Waves in Hollow Circular Cylinders, I. Analytical Foundation,,*The Journal of the Acoustical Society of America, 1959, **31**(5): p. 568-573.

5. Gazis, D. C., *Three-Dimensional Investigation of the Propagation of Waves in Hollow Circular Cylinders, II. Numerical Results,* The Journal of the Acoustical Society of America, 1959, **31**(5): p. 573-578.

6. Zemanek, J., Jr., *An Experimental and Theoretical Investigation of Elastic Wave Propagation in a Cylinder,* The Journal of the Acoustical Society of America, 1972, **51**(1): p. 265-283.

7. Li, J. and Rose, J. L., *Excitation and Propagation of Non-Axisymmetric Guided Waves in a Hollow Cylinde,.* The Journal of the Acoustical Society of America, 2001, **109**(2): p. 457-464.

8. Li, J. and Rose, J. L., *Angular-Profile Tuning of Guided Waves in Hollow Cylinders Using a Circumferential Phased Array,* IEEE Transactions on Ultrasonics, Ferroelectrics, and Frequency Control, 2002, **49**(12): p. 1720-1729.

9. Li, J. and Rose, J. L., *Natural Beam Focusing of Non-Axisymmetric Guided Waves in Large-Diameter Pipes,* Ultrasonics, 2006, **44**(1): p. 35-45.

10. Sun, Z., Zhang, L., and Rose, J. L., *Flexural Torsional Guided Wave Mechanics and Focusing in Pipe,* Journal of Pressure Vessel Technology, 2005, **127**: p. 471-478.

11. Viktorov, I. A., *Rayleigh and Lamb Waves, Physical Theory and Applications,* Ultrasonic Technology, ed. Lewis Balamuth, 1967, New York: Plenum Press, 154.

12. Liu, G. and Qu, J., *Guided Circumferential Waves in a Circular Annulus,* Journal of Applied Mechanics, 1998, **65**: p. 424-430.

13. Zhao, X. and Rose, J. L., *Guided Circumferential Shear Horizontal Waves in an Isotropic Hollow Cylinder,* The Journal of the Acoustical Society of America, 2004, **115**(5): p. 1912-1916.

14. Rose, J. L., *Ultrasonic Waves in Solid Media,* 1st ed. 1999, Cambridge, UK: Cambridge University Press, 454.

15. Valle, C., Niethammer, M., Qu, J., and Jacobs, L. J., *Crack Characterization Using Guided Circumferential Waves,* The Journal of the Acoustical Society of America, 2001, **110**(3): p. 1282-1290.

16. Van Velsor, J.K., Rose, J. L., and Nestleroth, J. B. *Coating Disbond Detection in Pipe Using Circumferentially-Oriented Ultrasonic Guided Waves,* in *ASNT Fall Conference and Quality Testing Show,* Nov. 2007, Las Vegas, NV: ASNT.

17. Hirao, M. and Ogi, H., *An SH-wave EMAT Technique for Gas Pipeline Inspection,* NDT&E International, 1999, **32**: p. 127-132.

18. Satyarnarayan, L., Chandrasekaran, J., Maxfield, B., and Balasubramaniam, K., *Circumferential Higher Order Guided Wave Modes for the Detection and Sizing of Cracks and Pinholes in Pipe Support Regions,* NDT&E International, 2008, **41**: p. 32-43.

19. Liu, G. and Qu, J., *Transient Wave Propagation in a Circular Annulus Subjected to Transient Excitation on its Outer Surface,* The Journal of the Acoustical Society of America, 1998, **104**(3): p. 1210-1220.

20. Li, Z. and Berthelot, Y. H., *Propagation of Transient Ultrasound in Thick Annular Waveguides: Modeling, Experiments, and Application,* NDT&E International, 2000, **33**: p. 225-232.

21. Valle, C., Qu, J., and Jacobs, L. J., *Guided Circumferential Waves in Layered Cylinders,* International Journal of Engineering Sciences, 1999, **37**: p. 1369-1387.

22. Towfighi, S., Kundu, T., and Ehsani, M., *Elastic Wave Propagation in Circumferential Direction in Anisotropic Cylindrical Curved Plates,* Journal of Applied Mechanics, 2002, **69**: p. 283-291.

23. Jiandong, Y., Bin, W., and Cunfu, H., *Guided Circumferential Waves in Orthotropic Cylindrical Curved Plate and the Mode Conversion by the End-Reflectio.* Applied Acoustics, 2007, **68**: p. 594-602.

24. Nestleroth, J. B. and Alers, G. A., *Enhanced Implementation of MFL Using EMAT Sensors to Detect External Coating Disbondment*, in *PRCI Contract PR-3-9715 Final Report,* 2002, Technical Toolboxes: Houston, TX, pp. 71.

25. Nestleroth, J. B. and Van Velsor, J. K., *Augmenting MFL Tools with Sensors that Assess Coating Condition*, in *DOT Contract No. DTPH56-06-T-000019 Final Report,* 2009, U. S. Department of Transportation, Pipeline and Hazardous Materials Safety Administration, pp. 67.

26. Aaron, J., Gore, J., Dalton, R., Eaton, S., Bowles, A., Thomas, O., and Jarman, T., *Development of an EMAT In-Line Inspection System for Detection, Discrimination, and Grading of Stress Corrosion Cracking in Pipelines*, in *DOE Award No. DE-FC26-01NT41154 Annual Technical Progress Report,* 2003, Tuboscope Pipeline Services: Houston, TX, pp. 49.

27. Al-Qahtani, H., Beuker, T., and Damaschke, J. *In-Line Inspection with High-Resolution EMAT Technology Crack Detection and Coating Disbondment,* in *Proceedings of 20th International Conference on Pipeline Pigging, Integrity Assessment and Repair,* 2008, Houston, TX.

28. Rose, J. L., *Basic Physics in Diagnostic Ultrasound,* 1979: John Wiley & Sons, New York.

29. Yu, L., Giurgiutiu, V., and Kendall, J. R. *Omnidirectional Guided Wave PWAS Phased Array for Thin-Wall Structure Damage Detection,* in *Sensors and Smart Structures Technologies for Civil, Mechanical, and Aerospace Systems 2007,* San Diego, CA: Proceedings of the SPIE.